# Schmid Factor Crack Propagation and Tracking Crystallographic Texture Markers of Microstructural Condition in Direct Energy Deposition Additive Manufacturing of Ti-6Al-4V

Alec I. Saville<sup>1</sup>, Jake T. Benzing<sup>2</sup>, Sven C. Vogel<sup>3</sup>, Jessica Buckner<sup>4</sup>, Collin Donohoue<sup>5</sup>, Andrew B. Kustas<sup>4</sup>, Adam Creuziger<sup>6</sup>, Kester D. Clarke<sup>1</sup>, Amy J. Clarke<sup>1</sup>

<sup>1</sup>Colorado School of Mines, Golden, CO
<sup>2</sup>National Institute of Standards and Technology, Boulder, CO
<sup>3</sup>Los Alamos National Laboratory, Los Alamos, NM
<sup>4</sup>Sandia National Laboratory, Albuquerque, NM
<sup>5</sup>Lockheed Martin, Lakewood, CO
<sup>6</sup>National Institute of Standards and Technology, Gaithersburg, MD

#### Abstract

Metallic additive manufacturing (AM) provides a customizable and tailorable manufacturing process for new engineering designs and technologies. The greatest challenge currently facing metallic AM is maintaining control of microstructural evolution during solidification and any solid state phase transformations during the build process. Ti-6Al-4V has been extensively surveyed in this regard, with the potential solid state and solidification microstructures explored at length. This work evaluates the applicability of previously determined crystallographic markers of microstructural condition observed in electron beam melting powder bed fusion (PBF-EB) builds of Ti-6Al-4V in a directed energy deposition (DED) build process. The aim of this effort is to elucidate whether or not these specific crystallographic textures are useful tools for indicating microstructural conditions in AM variants beyond PBF-EB. Parent  $\beta$ -Ti grain size was determined to be directly related to  $\alpha$ -Ti textures in the DED build process, and the solid state microstructural condition could be inferred from the intensity of specific  $\alpha$ -Ti orientations. Qualitative trends on the as-solidified  $\beta$ -Ti grain size was also determined to be related to the presence of a fiber texture. and proposed as a marker for as-solidified grain size in any cubic metal melted by AM. Analysis of the DED Ti-6Al-4V build also demonstrated a near complete fracture of the build volume, suspected to originate from accumulated thermal stresses in the solid state. Crack propagation was found to *only* appreciably occur in regions of slow cooling with large  $\alpha + \beta$  colonies. Schmid factors for the basal and prismatic  $\alpha$ -Ti systems explained the observed crack pathway, including slower bifurcation in colonies with lower Schmid factors of both slip systems. Colony morphologies and localized equiaxed  $\beta$ -Ti solidification were also found to originate from build pauses during production and uneven heating of the build edges during deposition. Tailoring of DED Ti-6Al-4V microstructures with the insight gained here is proposed, along with cautionary insight on preventing unplanned build pauses to maintain an informed and controlled thermal environment for microstructural control.

#### 1. Introduction

Metallic additive manufacturing (AM) enables the production of custom geometry parts and rapid design iteration during the overall design process [1–3]. This enables manufacturing without the

requirement for extensive tooling, long production lead times, or removing excess material in substantial quantities, drastically reducing unit time and production cost. Three primary types of metallic AM have come to prominence as defined by ASTM: laser powder bed fusion (PBF-LB), electron beam melting powder bed fusion (PBF-EB), or directed energy deposition (DED) [4]. Other AM build processes exist (e.g., binder jetting or cold spraying), but these do not typically employ a sequential melting process such as those previously described. Regardless of build process, metallic AM struggles to guarantee repeatable microstructural control during solidification and in solid state transformations throughout a build process [5,6]. This results in many AM parts performing outside of specification, relegating the manufacturing technique to low-risk applications [2,7]. Therefore, there is an urgent need to develop methods of microstructural control in metallic AM to realize the time and cost savings this manufacturing technique can bring to higher-risk applications.

Additively manufactured Ti-6Al-4V, an  $\alpha + \beta$  titanium alloy, has been the focus of many microstructural studies. This has been due to the potential savings and design advantages AM can realize for the biomedical and aerospace industries where Ti-6Al-4V is commonly implemented [4]. AM Ti-6Al-4V solidifies as the high temperature body centered cubic (BCC)  $\beta$ -Ti phase with a  $\{001\}_{\beta}$  texture parallel to the solidification direction [8,9]. The  $\{001\}_{\beta}$  texture is primarily associated with columnar solidification, described more below. The solidification direction is often aligned with the build direction, but not always [10–12]. The solidification morphology of  $\beta$ -Ti is dictated by the thermal gradient (G) and solidification velocity (V) of the solid-liquid interface [13]. Both factors are sensitive to build parameters such as scan strategy, feedstock, and heat source [14]. The majority of AM Ti-6Al-4V solidifies with  $\beta$ -Ti in a columnar dendritic morphology [6,8,9,12,14–18], though the scale of this microstructure is a function of the cooling rate (G x V) [13]. Generally, DED builds have the coarsest solidification microstructures, followed by PBF-LB builds and finally PBF-EB. Columnar dendritic microstructures are highly directional both at the microstructural and crystalline scales irrespective of alloy system, potentially leading to anisotropic material properties [2,6]. Thus, previous work has pursued achieving equiaxed dendritic solidification across alloys, especially Ti-6Al-4V.

Traditional inoculation techniques to achieve equiaxed dendritic solidification for aluminum and other alloy types are typically ineffective in Ti-6Al-4V. Some success has been found with oxide additions and targeted solute additions [19–25]. However, bimodal equiaxed-columnar dendritic and close to pure equiaxed dendritic solidification has been achieved through careful manipulation of build thermal conditions. Previous work discovered changing scan strategy to reduce thermal gradients and increasing solidification velocity promoted the formation of finer columnar and mixed columnar-equiaxed  $\beta$ -Ti in Ti-6Al-4V. This was confirmed by  $\beta$ -Ti reconstruction, solidification modelling, and microstructural characterization [10,26,27] for Ti-6Al-4V, and has been explored more broadly for general AM build processes [28,29].

Upon cooling below ~ 980 °C, Ti-6Al-4V  $\beta$ -Ti transforms into the lower temperature  $\alpha$ -Ti phase. This hexagonal close packed (HCP) phase takes on one of 12 different orientations (each known as a variant) according to the Burgers Orientation Relationship (OR) given by  $\{0001\}_{\alpha} \parallel \{110\}_{\beta}$  and  $< 11\overline{2}0 >_{\alpha} \parallel < 111 >_{\beta} [30]$ . It is worth noting at ~ 25 °C and assuming equilibrium conditions, Ti-6Al-4V is expected to consist of 90%  $\alpha$ -Ti and 10%  $\beta$ -Ti by phase fraction. AM Ti-6Al-4V often exhibits lower  $\beta$ -Ti phase fractions. The preferential selection of one or a few  $\alpha$ -Ti variants is known as variant selection. This can lead to anisotropic properties if sufficient variant

selection is achieved or different variants in other parent grains align coincidentally [15,16]. From this transformation process,  $\alpha$ -Ti takes on different microstructural morphologies depending on the cooling rate and parent  $\beta$ -Ti grain sizes [31]. Faster cooling rates through the  $\beta$ -Ti transus will produce martensitic  $\alpha'$  and suppress the presence of any equilibrium high temperature  $\beta$ -Ti [18,32–35]. This is often seen in PBF-LB build processes. Intermediate cooling rates (~ 50 °C/sec) [31,32] will typically produce Widmanstätten  $\alpha$ -Ti in basketweave or elongated plate morphologies and a reduced  $\beta$ -Ti phase fraction. Slower solid state cooling rates will result in characteristic  $\alpha + \beta$  colony microstructures Ti-6Al-4V is known for. These cooling rates are sensitive to the size of parent  $\beta$ -Ti grains, with smaller grains exhibiting smaller mean-free paths for diffusion, and thereby requiring faster cooling rates for non-colony microstructures [31]. Widmanstätten  $\alpha$ -Ti is often observed in PBF-EB and DED build processes [11,36], while colonies are most commonly found in PBF-EB builds [10,18]. It is important to note these generalizations are not all inclusive, as PBF-EB builds can still produce martensitic microstructures and DED colony structures when thermal conditions are sufficiently altered. Finer parent  $\beta$ -Ti grain sizes have also been linked to the formation of  $\alpha + \beta$  colony microstructures. This was attributed to the reduced mean-free path for diffusion in smaller grains enabling closer to equilibrium partitioning [10].

Preferential orientation (also known as crystallographic texture) of  $\alpha$ -Ti crystals in AM adds another layer of complexity to the microstructural evolution of AM Ti-6Al-4V. Faster cooling rates typically reduce  $\alpha$ -Ti textures, while slower cooling rates can produce up to 4x the preferential orientations in the solid state microstructure [10]. Texture has been shown to change minimally as a function of build height, but local thermal changes can still result in deviations in preferred orientations of either parent or product phases. Considering the Burgers OR is almost always followed during the  $\beta \to \alpha$  transformation, the orientation and size of the as-solidified  $\beta$ -Ti likely also influences the product  $\alpha$ -Ti texture.

The combination of variable solidification and solid state microstructures with changes in crystallographic texture demonstrate how challenging microstructural control is in AM builds of Ti-6Al-4V. In a step towards this goal, previous work on PBF-EB Ti-6Al-4V found specific preferential  $\alpha$ -Ti orientations was associated with both changes in parent  $\beta$ -Ti grain size and the morphology of the  $\alpha$ -Ti microstructure [10]. The presence of a  $\{01\overline{1}2\}_{\alpha}$  fiber texture parallel to the build direction was found consistently in the presence of finer parent  $\beta$ -Ti grains and with  $\alpha$  + β colonies formed by diffusion from slower cooling rates. Moreover, the intensity of this fiber texture was found to correspond directly to the quantity of colonies in the solid state microstructure and inversely to the parent  $\beta$ -Ti grain size. Conversely, a  $\{11\overline{2}0\}_{\alpha}$  fiber texture parallel to the build direction was observed for faster cooling rate solid state microstructures. It was suggested the  $\{01\overline{1}2\}_{\alpha}$  fiber texture could be used as a marker of microstructural condition (e.g., estimate the size of as-solidified  $\beta$ -Ti and the type of solid state microstructure present) via techniques such as X-ray diffraction (XRD), bypassing the need for extensive characterization work in validating build quality. However, it was not clear whether the  $\{01\overline{1}2\}_{\alpha}$  fiber corresponded to both parent  $\beta$ -Ti grain size and solid state microstructure, or if it was a specific marker of microstructural condition to PBF-EB build processes [10].

This work expands the previously mentioned PBF-EB efforts by exploring the relationship between crystallographic texture and microstructure in DED Ti-6Al-4V. DED build processes are typically employed for larger build volumes and higher throughputs, making this AM variant more

applicable to on-demand structural applications than PBF-EB or PBF-LB. DED also enables the elucidation of if the  $\{01\overline{1}2\}_{\alpha}$  fiber texture parallel to the build direction is a hallmark of finer  $\beta$ -Ti grains and/or diffusional microstructures, and if this marker of microstructural condition can be used for other AM processes besides PBF-EB.

# 2. Material and Methods

#### 2.1 Material Production

DED Ti-6Al-4V samples were extracted from the larger bowl build volume observed in Figure 1a via electrical discharge machining (EDM). The full build geometry was produced on a modified HASS\* VF2-TR 5 computer numerical control (CNC) machine equipped with a tungsten inert gas (TIG) welding torch at Sandia National Laboratory (SNL). The exact thermal history of the build was not known before analysis. A specific real space reference frame was selected according to ASTM standards to relate crystallographic texture information to the AM build process [37]. The CNC machine deposited material with a layer height of 3 mm and traversed at 0.15 m/min using 1.143 mm thick Ti-6Al-4V wire fed at 0.725 mm/min. The majority of the build was deposited using a traversal in the XY plane from the inside diameter to the outside diameter of the bowl as seen in Figure 1b. Once the inner and outer diameters were completed, the outer rim was applied with vertical traversal along the Z-axis (Figure 1b). The TIG welding setup employed a 40 A current and argon shielding gas with a flow rate of 10 L/min. Though material was deposited in linear traversals, the rotation of the build volume proceeded along the X-axis. Thus, akin to traditional welding, the X-axis can be thought of here as the travel direction for deposition.

Four primary samples from the full build height were extracted for investigation in this work. Two samples towards the bottom quarter of the build were extracted constituting 0-30 mm and 30-50 mm in build height respectively. The other two were extracted near the top of the build volume, covering build heights between ~ 80-100 mm and 100-130 mm (the build finish). The outer rim was sectioned from the 100-130 mm specimen for analysis of the different traversal path. Each primary sample was sectioned in half along the YZ-plane, with the right half (positive X-axis section) mounted for metallography and the left half for measuring crystallographic texture.

\_

<sup>\*</sup>Certain commercial equipment, instruments, or materials are identified in this paper in order to specify the experimental procedure adequately. Such identification is not intended to imply recommendation or endorsement by the National Institute of Standards and Technology, nor is it intended to imply that the materials or equipment identified are necessarily the best available for the purpose.

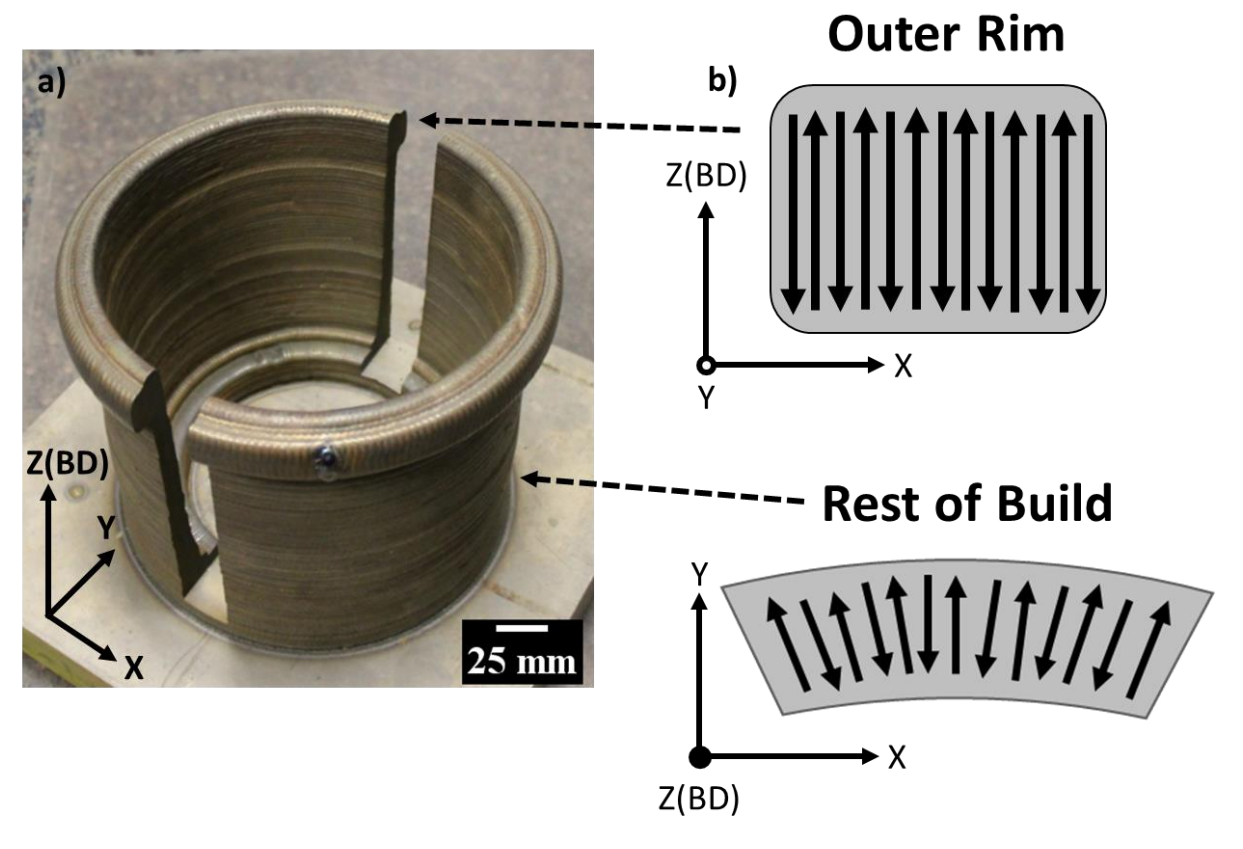


Figure 1: a) The full DED build volume produced at SNL with the real space reference frame employed here overlaid for reference. b) The traversal paths of material deposition for the outer rim (top) and the remaining portion of the build (bottom). Note the graphics in b) have different orientations relative to the given reference frame, where the build direction is given by BD.

#### 2.2 Microstructural Characterization

The right half of each primary specimen was mounted in copper-containing conductive mounting bakelite for scanning electron microscopy (SEM) characterization. Metallographic preparation consisted of using 800 grit grinding paper, 9  $\mu$ m diamond solution, and 9.8 pH 0.05  $\mu$ m colloidal silica on a rotary auto polisher to achieve a mirror finish. Etching was not required given the chemical-mechanical etching achieved with the 0.05  $\mu$ m colloidal silica. SEM characterization was completed on a Tescan\* S8000 SEM using an accelerating voltage of 20 kV and 11 nA probe current. Energy dispersive spectroscopy was completed using an EDAX\* Octane Elect Plus with 5 keV accelerating voltage and 11 nA probe current.

# 2.3 Measuring Crystallographic Texture

The left half (negative X-axis) of each primary specimen was analyzed at the High-Pressure-Preferred-Orientation (HIPPO) neutron diffraction beamline at the Los Alamos Neutron Science

\*Certain commercial equipment, instruments, or materials are identified in this paper in order to specify the experimental procedure adequately. Such identification is not intended to imply recommendation or endorsement by the National Institute of Standards and Technology, nor is it intended to imply that the materials or equipment identified are necessarily the best available for the purpose.

Center (LANSCE) at Los Alamos National Laboratory (LANL). These measurements used ambient conditions with a 10 mm diameter incident beam and 15 minute analysis period. Three scans were completed on each primary specimen along the Z-axis to observe any change in texture with build height. Two scans up the Z-axis were also completed on the outer rim sectioned for the top 100-130 mm build height specimen. Collected data was processed using the Material Analysis Using Diffraction (MAUD) software with a 7.5° orientation distribution function (ODF) resolution in accordance to previously documented methods [38]. The output pole figures were processed using MTEX 5.70 with ODF's set to a 5° resolution [39]. The 7.5° ODF resolution in MAUD has been shown to accurately capture orientations from the Rietveld refinement process without introducing artificial sharpening of orientations for this data. A 5° ODF resolution in MTEX meanwhile has demonstrated similar consistency to that shown for the resolution selected in MAUD. The MTEX ODF calculation process is different than that of MAUD however, necessitating a different resolution value. Both programs can have their ODF resolutions tweaked as needed according to the quality and type of input data. It is recommended researchers try multiple resolutions in MAUD to find the right value for their dataset, and calculate the optimal resolution size using kernel calculations outlined in the MTEX documentation.

Crystallographic texture for the right half (positive X-axis) section of each primary specimen was analyzed using electron backscatter diffraction (EBSD) on a Gemini field emission SEM with a 20 kV accelerating voltage, 11 nA probe current, 3  $\mu$ m step size, and a working distance of 22 mm. All specimens were sectioned into two halves along the XY-plane to enable easier manipulation during metallographic preparation. Individual EBSD scans ~ 1100  $\mu$ m x 1000  $\mu$ m were acquired and stitched together into centimeter scale composite maps of 65-75% of each primary specimens surface area. EBSD data was processed using MTEX 5.70 for inverse pole figure (IPF) maps and other figure generation, while orientation analysis employed 5° ODF resolutions [40].  $\beta$ -Ti reconstructions were completed using MTEX 5.70's parent grain reconstruction algorithm employing the identification of triple points and voting algorithms to group  $\alpha$ -Ti orientations into the correct parent grains [41]. A 5° misorientation threshold was defined for specifying unique parent  $\beta$ -Ti grains during reconstruction. All Euler angles were processed according to the Bunge convention [42].

Centimeter scale EBSD maps were required to capture the expected multiple-millimeter wide parent  $\beta$ -Ti grains present in the DED Ti-6Al-4V specimens. This also ensures the acquisition of enough data points to acquire representative textures from EBSD and confirm these findings with neutron diffraction. Employing 4 mm x 4 mm or smaller EBSD maps would likely survey at maximum 2-3  $\beta$ -Ti grains as evidenced from previous work [12,43], leading to artificially inflated texture values not representative of the full microstructure.

Orientation simulations were completed in MTEX 5.70 employing a 5° halfwidth for simulated ODF's and orientations.

#### 3. Results

#### 3.1 Microstructural Characterization

Microstructural characterization of the four primary DED Ti-6Al-4V specimens identified four dominant microstructural morphologies throughout the build volume. These included fine and coarse Widmanstätten basketweave morphologies (Figure 2a and 2b respectively). A distinct

categorization between these two microstructures was established considering the different cooling rates required to form the distinct scales of the same morphology. Two other morphologies, elongated "bow-tie" colonies (Figure 2c) and colonies with high aspect ratio  $\alpha$ -Ti plates (Figure 2d) were also observed. Each morphology constituted a layer of the build between each 3 mm thick build layer in a tiered pattern akin to that of previous DED work by Kelly and Kampe [43]. These morphologies can also be predicted by solid state phase field modelling of AM Ti-6Al-4V [32].

Coarse traditional  $\alpha + \beta$  colony structures were found predominantly at the edges of the build volume (Figure 2e) and in local regions in between the four primary morphologies (Figure 2f). The size of these microstructures indicates considerably slower cooling in selected regions of the build volume. The origin of these microstructures will be discussed more in Section 4.1.2 Coarse Colony Microstructures.

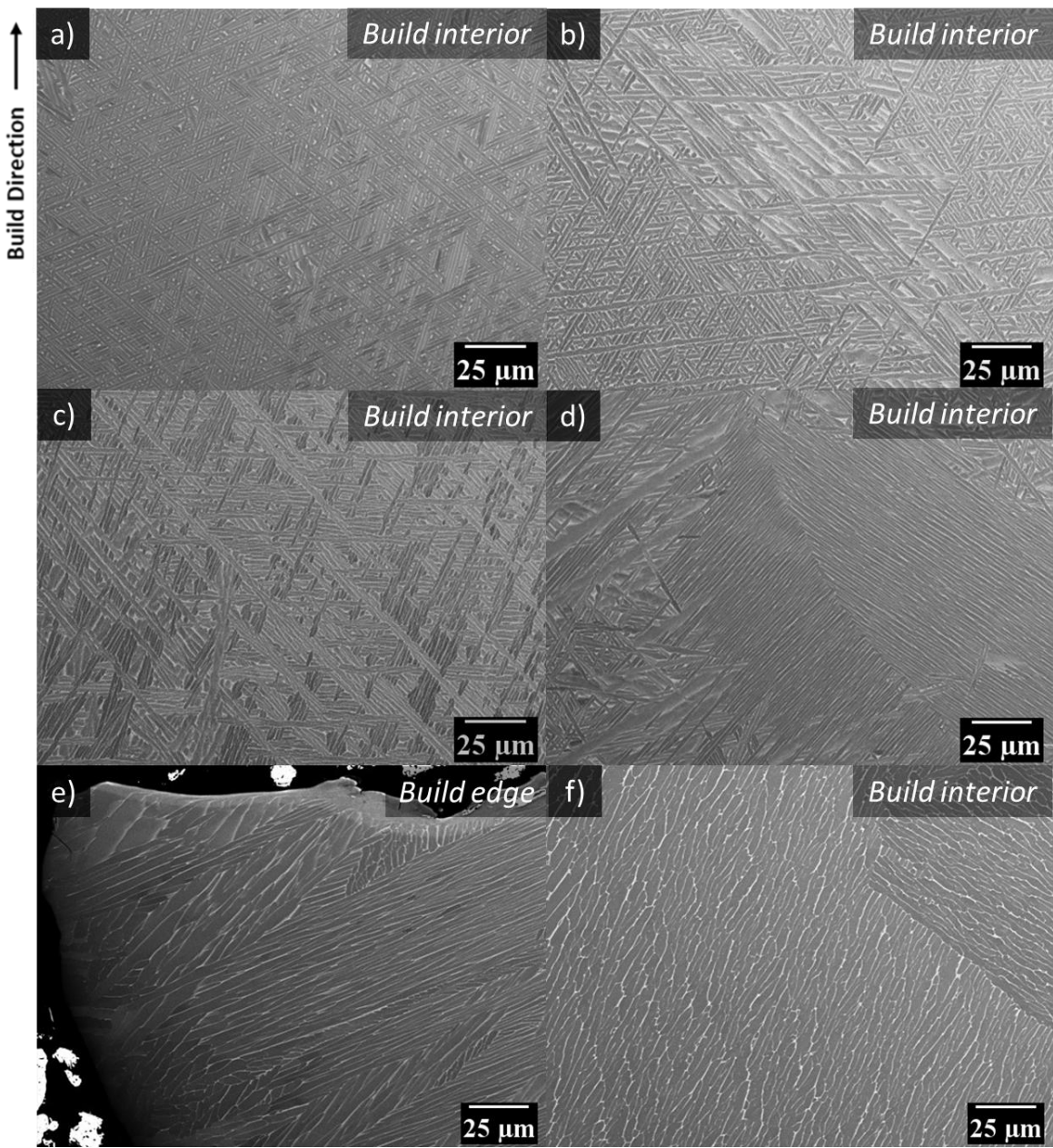


Figure 2: SEM backscatter electron micrographs of DED Ti-6Al-4V microstructures. Four predominant microstructures including, fine basketweave (a), coarse basketweave (b), elongated "bow-tie" colonies (c), and high-aspect ratio plate colonies (d) were observed in a tiered structure throughout the build. Coarse traditional  $\alpha + \beta$  colonies were observed at the edges (e) and internal to the build (f), indicating considerably variable cooling rates throughout the DED build process.

#### **3.2 EBSD**

#### 3.2.1 0-30 mm Build Height

Large-scale EBSD of material in the first specimen was completed using a 19 x 5 mm map centered at  $\sim$  3 mm in build height (Error! Reference source not found.a). All EBSD data, whether IPF maps or other graphical representations, are reported with the X-axis into the page, build direction (Z-axis) up the page, and Y-axis from right to left. Pole figures are represented in the standard reference frame described in Figure 1a. This detail is important for understanding how to align EBSD data and pole figures correctly. An  $\alpha$ -Ti IPF map of the 19 x 5 mm area demonstrates large multi-millimeter prior  $\beta$ -Ti grains containing regions of distinct  $\alpha$ -Ti orientations. Bands of high aspect ratio plate  $\alpha$ -Ti can also be observed every  $\sim$  3 mm in the build height, corresponding well to the layer thickness of the build and the previously described layered microstructures. The majority of the microstructure consists of the four previously described morphologies as evidenced by the patterning of  $\alpha$ -Ti orientations throughout the map.

Kernel average misorientation (KAM) analysis of the  $\alpha$ -Ti EBSD data demonstrated considerably high pixel-to-pixel misorientations inside the predominantly basketweave microstructure (Figure 4a). Grain boundary  $\alpha$ -Ti and any colony microstructures exhibited lower KAM misorientations, but this may not be representative of local misorientations. This is attributed to the EBSD step size being larger than the average  $\beta$ -Ti rib in colony microstructures, and thus unable to discern finer boundaries internal to diffusional portions of the microstructure. Regardless, the dominant microstructural morphology for  $\alpha$ -Ti can be easily observed in Figure 4a. It is important to note KAM maps are presented in this work for both the as-built and reconstructed as-solidified microstructures to note general trends. KAM values will *not* be presented to quantify aspects of the microstructure considering the challenges involved in extracting confident and quantifiable KAM values. This is especially true for finer  $\alpha$ -Ti microstructures and reconstructed  $\beta$ -Ti grains, where nuances in the data are lost during collection and processing (e.g., exact misorientations between parent  $\beta$ -Ti grains may be lost during reconstruction where some approximated orientations are represented).

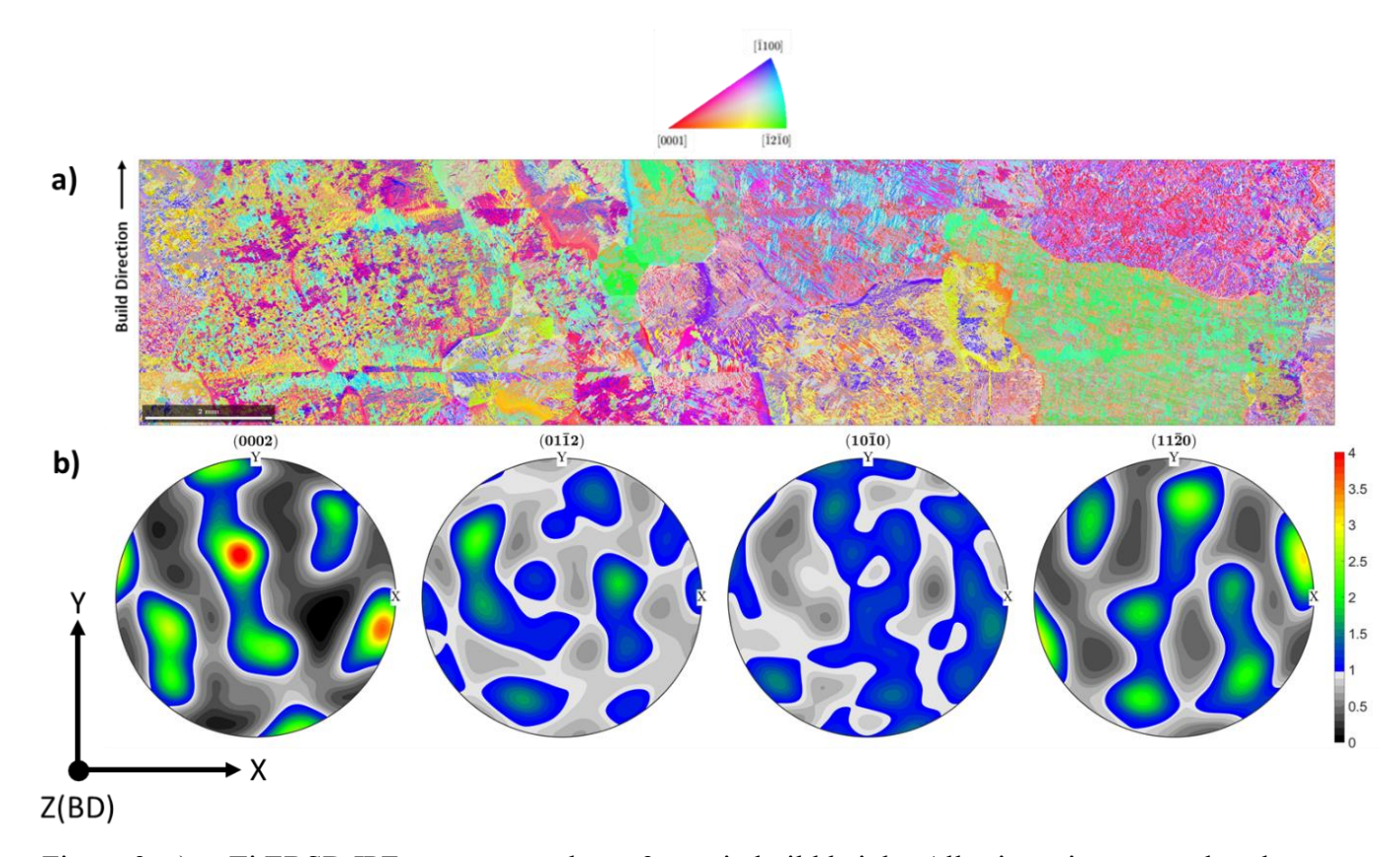


Figure 3: a)  $\alpha$ -Ti EBSD IPF map centered at  $\sim$  3 mm in build height. All orientations are colored with respect to the build direction (up the screen). b)  $\alpha$ -Ti pole figures from EBSD data illustrating the preferential orientation of  $\alpha$ -Ti within the build reference frame.

Preferential orientations of  $\alpha$ -Ti in this portion of the build are concentrated in specific clusters according to Figure 3Error! Reference source not found.b, indicative of the few  $\beta$ -Ti grains present having similar initial orientations. No presence of a  $\{01\overline{1}2\}_{\alpha}$  fiber texture was observed, with little to no preferential alignment of the  $(01\overline{1}2)_{\alpha}$  planes. Rather,  $(11\overline{2}0)_{\alpha}$  planes appear with a higher texture (2.5-3x multiples of random distribution, or m.r.d. for short). Though not of the same magnitude, increased texturing of  $(11\overline{2}0)_{\alpha}$  planes over  $(01\overline{1}2)_{\alpha}$  planes was found in microstructures with higher solid state cooling rates in PBF-EB Ti-6Al-4V [10].

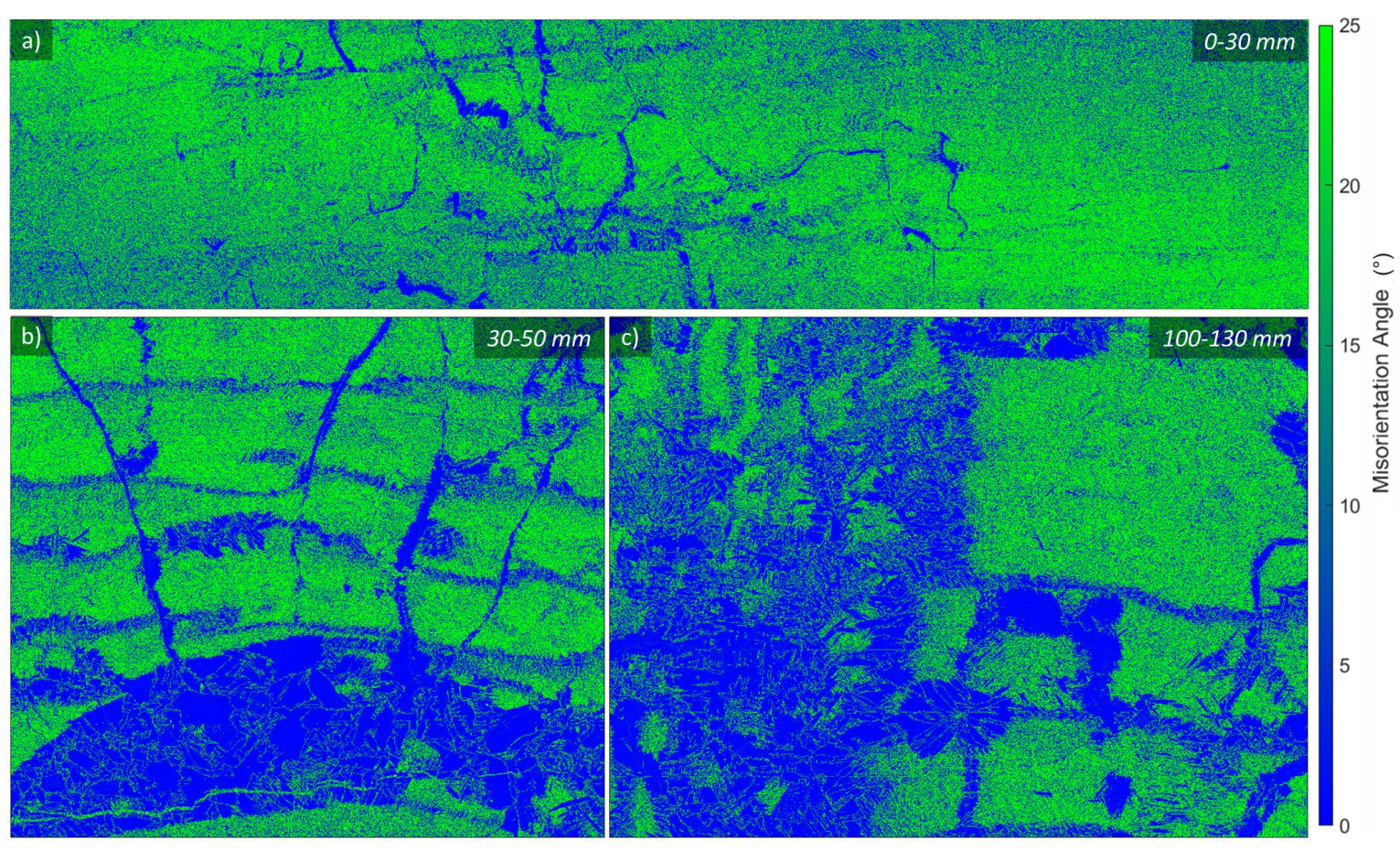


Figure 4: KAM maps measuring the as-built  $\alpha$ -Ti misorientation for neighboring pixels at a) 0-30 mm, b) 30-50 mm in build, and c) 100-130 mm in build height. Portions of the microstructure containing colony microstructures exhibited considerably lower KAM misorientations than those with a basketweave morphology. This was attributed to the EBSD step size being larger than the finest boundaries for diffusional microstructures. However, the dominant  $\alpha$ -Ti microstructural morphology for each location can easily be determined from these KAM maps.

Reconstruction of the as-solidified  $\beta$ -Ti microstructure [41] confirms the presence of large multimillimeter  $\beta$ -Ti grains, considerably larger than those found in PBF-EB (Figure 5a). The reconstructed parent grains at 0-30 mm build height do not illustrate a strong  $\{001\}_{\beta}$  orientation parallel to the build direction. This is further supported by illustrating the crystal orientations where most  $\beta$ -Ti grains are tilted into the page at  $\sim 30$ -40° angles (Figure 5b). Such crystal maps are generated using the Euler angles from EBSD data and aligning the data reference frame with the analyzed surface. KAM analysis of the reconstructed microstructure demonstrates limited misorientation within the solidified microstructure, but some grains contain points with  $\sim 10^\circ$  misorientations (Figure 6a). These predominantly correspond to the largest reconstructed  $\beta$ -Ti grain in the area surveyed, indicating potential residual stress leftover from solidification or grain misorientations below the threshold set when calculating grains in MTEX.

The same crystal orientations in Figure 5b are represented on pole figures in Figure 5c. These demonstrate the same parent  $\beta$ -Ti tilt but from different perspectives as previously clarified. This point is also reinforced by showing the same crystal tilt observed in Figure 5b next to the pole

figures in Figure 5c. A moderately strong (4x m.r.d.) quasi-cube texture (rotated ~ 20° off a typical cube texture) is observed via the  $(001)_{\beta}$  poles along the solidification direction. This indicates the  $\beta$ -Ti solidified in between the X-axis and build direction shortly after the build process began. The reconstruction results also suggest the linear traversal along the Y-axis did not significantly alter the  $\beta$ -Ti solidification direction. Rather, the travel direction/X-axis dominated how  $\beta$ -Ti oriented during solidification. Such solidification has also been predicted extensively in solidification simulations [32,44–47]. It is possible tilting of the TIG torch could also establish this crystallographic tilt by changing the direction of heat flow into the top surface. EBSD centered at ~ 20 mm build height returned similar orientations and microstructures, and is not included here for brevity.

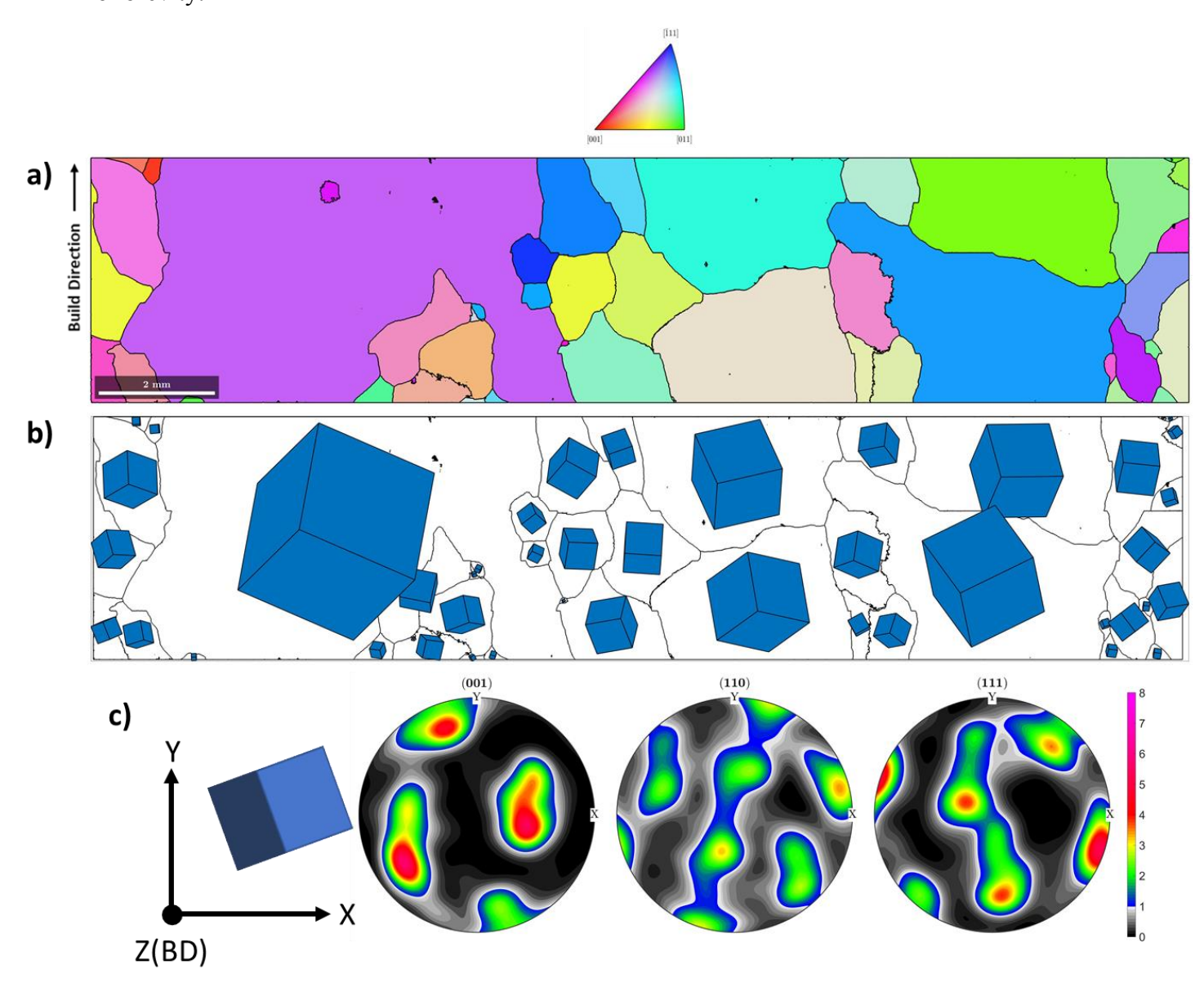


Figure 5: a) Reconstructed  $\beta$ -Ti IPF map clearly illustrating the presence of multi-millimeter sized grains throughout the surveyed area. All orientations colored with respect to the build direction. b) Crystal map illustrating the alignment of cubic  $\beta$ -Ti crystals within the surveyed area. Note the X-axis is into the screen for all spatial EBSD maps. c) Reconstructed EBSD  $\beta$ -Ti pole figures

illustrating the preferential tilt of the cubic crystals towards the X-axis of the reference frame. An example cube is illustrated to relate the dominant orientation of  $\beta$ -Ti in c) to the crystal map in b).

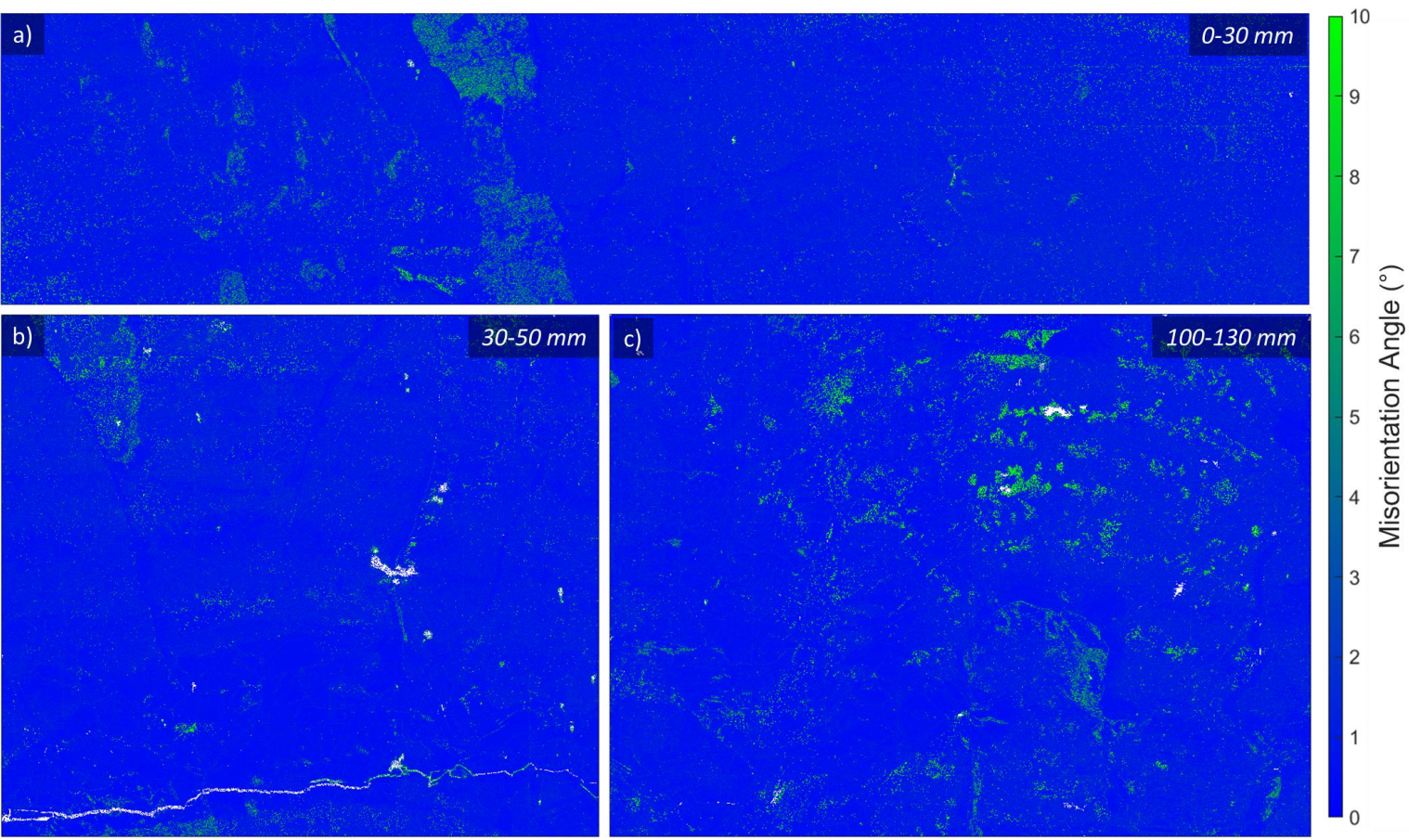


Figure 6: KAM maps measuring the reconstructed  $\beta$ -Ti misorientation for neighboring pixels at a) 0-30 mm, b) 30-50 mm, and c) 100-130 mm in build height. Reconstructed  $\beta$ -Ti KAM values were significantly less than those observed for the as-built  $\alpha$ -Ti microstructure due to the morphological differences of the two microstructures. Localized regions of higher KAM values ( $\sim$  10°) are observed throughout the build volume, but decrease in frequency near the fractured portion of the build. This potentially suggests a reduction of residual stress near the fracture site, or is indicative of different solidification conditions and solid state microstructures. Note the smaller color scale here than in Figure 4 indicating lower misorientation values.

# 3.2.2 30-50 mm Build Height

EBSD mapping between 30-50 mm build height centered at  $\sim$  40 mm was completed to observe any microstructural and texture changes. Figure 7a illustrates a 10 x 9 mm  $\alpha$ -Ti IPF map with large  $\beta$ -Ti grains obvious in the upper half of the surveyed area. The *entire* Y-axis width of the specimen was surveyed in this map. A coarsening of parent  $\beta$ -Ti grain size is apparent compared to the area surveyed in Figure 3Error! Reference source not found. Unlike in Figure 3aError! Reference source not found. however, the microstructure observed here is split between the aforementioned four morphologies and large  $\alpha + \beta$  colonies on the order of one millimeter. These  $\alpha + \beta$  colonies indicate drastically reduced solid state cooling rates and appear at the bottom of the surveyed area as regions of singular orientations. The faint outline of a crack can also be spotted at the base of

Figure 7a. This crack appears to propagate the entire width of the build volume and *only* travel through the coarse  $\alpha + \beta$  colony region, avoiding any basketweave morphologies. This will be discussed more in 4.3.1 Crack Propagation.  $\alpha$ -Ti KAM values again varied between the basketweave and diffusional (colony and grain boundary  $\alpha$ -Ti) morphologies as previously discussed (Figure 4b).

 $\alpha$ -Ti pole figures in Figure 7b demonstrate similar orientations for the  $\alpha$ -Ti phase at lower build heights, but with a slightly reduced texture. A more distinct concentration of the  $(0002)_{\alpha}$  planes also appears in Figure 7b, with preferential orientations in this pole figuring marking the corners of a square. These orientations will be further explored in Section 4.2.1 EBSD, but are potentially indicative of the Burgers OR assuming a  $\{001\}_{\beta}$  texture for the as-solidified  $\beta$ -Ti (Figure A 1 & Figure A 2). From here onward, this type of  $\alpha$ -Ti texture will be called the *12 variant texture*. This texture is also weakly present in **Error! Reference source not found.** Figure 3b. Neither a  $\{01\overline{1}2\}_{\alpha}$  fiber texture parallel to the build direction or a strong texturing of the  $(01\overline{1}2)_{\alpha}$  and  $(11\overline{2}0)_{\alpha}$  poles appear aligned to the center of the square outlined in the  $(0002)_{\alpha}$  pole figure. An increased width of the discrete *12 variant texture* also appears present, potentially indicative of the beginning of a  $\{01\overline{1}2\}_{\alpha}$  or  $\{11\overline{2}0\}_{\alpha}$  fiber texture along the solidification direction.

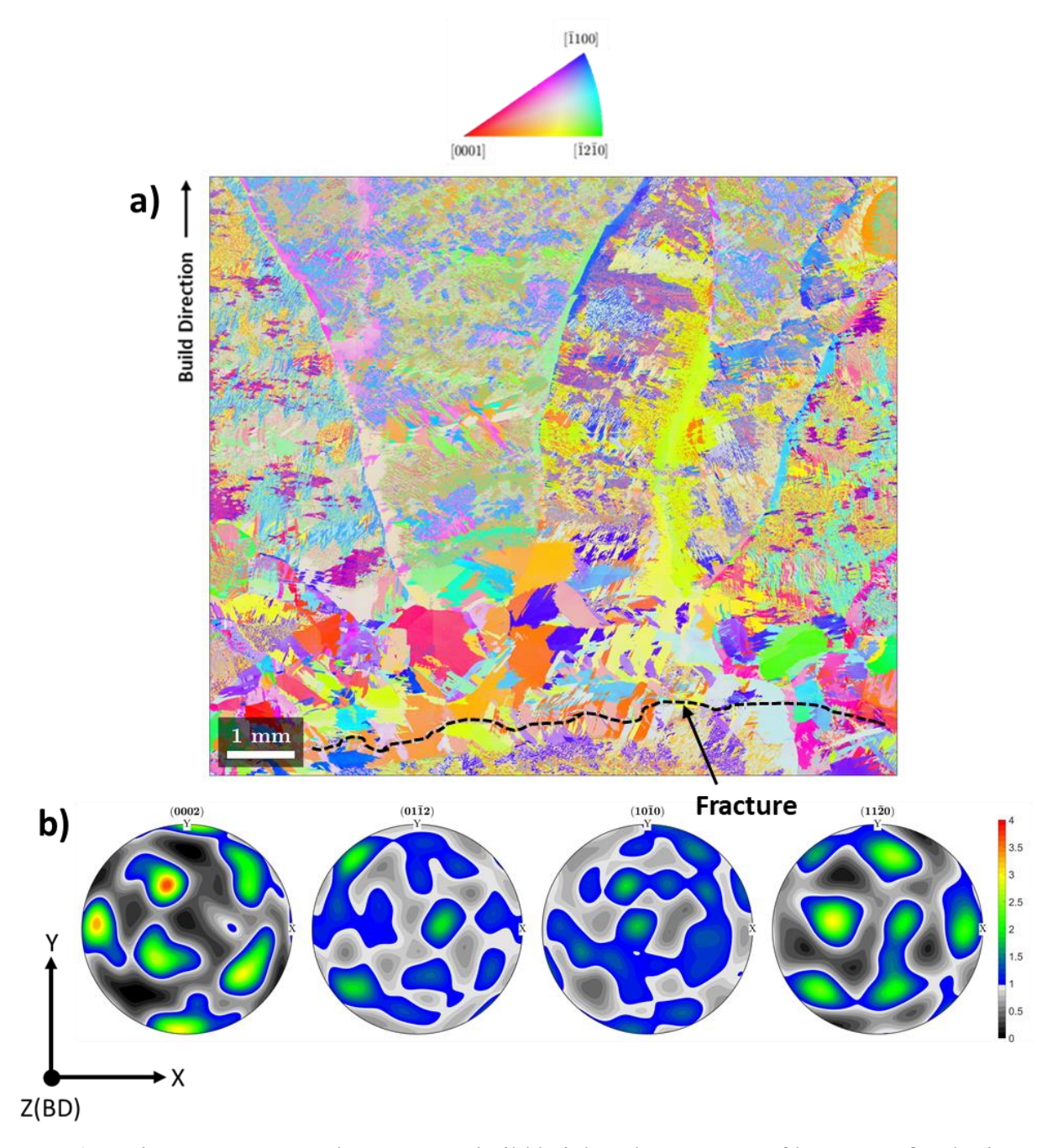


Figure 7: a)  $\alpha$ -Ti IPF map centered at  $\sim$  40 mm build height. The presence of large  $\alpha + \beta$  colonies can be seen towards the bottom of the surveyed area along with a crack outline (black dashed line). All orientations colored with respect to the build direction. b) EBSD  $\alpha$ -Ti pole figures illustrating a comparable texture to that seen in **Error! Reference source not found.**b. The square of orientations in the  $(0002)_{\alpha}$  pole figure suggests the presence of a  $\{001\}_{\beta}$  solidification texture.

Reconstructing the parent  $\beta$ -Ti microstructure for this area returns the data presented in Figure 8. The reconstructed  $\beta$ -Ti IPF map in Figure 8a shows the  $\beta$ -Ti grains solidified with  $(001)_{\beta}$  poles closer to the build direction than lower in the build. This is confirmed by Figure 8b and Figure 8c, where a rotated cube texture  $\sim 10^{\circ}$  off the build direction dominates the parent phase orientations.

The alignment of the  $(0002)_{\alpha}$  and  $(001)_{\beta}$  poles indicates the Burgers OR governed the majority of the transformation process for this region. Curiously, analyzing the KAM map for this reconstructed microstructure shows this region had significantly less point-to-point misorientation than at the start of the build (Figure 6b). This could be indicative of stress relaxation from the fracture identified in Figure 7a, the coarsening of the parent  $\beta$ -Ti grain size, or another as-of-yet unidentified factor.

Further inspection of Figure 8a shows a mixture of parent  $\beta$ -Ti grain sizes. Smaller, equiaxed  $\beta$ -Ti grains appear at the specimen edges, while more traditional columnar dendritic grains fan out above these grains. This is not obvious in KAM analysis, suggesting limited misorientations in the as-solidified microstructure (Figure 6b). The columnar grains here appear similar to single-pass weld microstructures considering the  $\beta$ -Ti grains fan out along thermal gradients angled away from the build direction. The BCC crystals are also aligned much closer to the build direction, indicating the max thermal gradient was along the build direction and not 30-40° off. Such orientations hint at different thermal conditions during solidification. Further discussion on this point will be covered later in Section 4.1.2 Coarse Colony Microstructures, but such a microstructure is indicative of deposition pauses during the build process.

Fanning out of columnar grains typically occurs at lower build heights at the start of deposition, not higher in the build. The presence of equiaxed  $\beta$ -Ti grains also suggests drastically reduced thermal gradients or higher solidification velocities to achieve such morphologies. These grains additionally solidified with their  $(001)_{\beta}$  poles far from the build direction, again reinforcing the notion these were formed via equiaxed solidification (Figure 8b). This is in contrast to the more aligned columnar grains. Some grains near the top of the equiaxed region begin to take on the  $\beta$ -Ti orientation of the large columnar grain above, potentially indicating competitive growth occurred locally during solidification. It is also worth noting that though these grains are being classified as "equiaxed" here, they scale on the order of millimeters. Such grain sizes are still larger than many columnar grains observed in PBF-LB and PBF-EB. A second but less prominent instance of these equiaxed grains was also observed at ~ 30 mm in build height (Figure A 3).

 $\beta$ -Ti reconstruction more clearly illustrates the location and extent of the cracking phenomenon. The crack originates within the equiaxed region on the outer diameter of the build (positive Y-axis, left side of the IPF map) and stops propagating just shy of the inner diameter (right side of the IPF map). The crack path evolves internally to the large  $\beta$ -Ti grain, indicating crack growth likely occurred after the  $\beta \to \alpha$  transformation had completed.

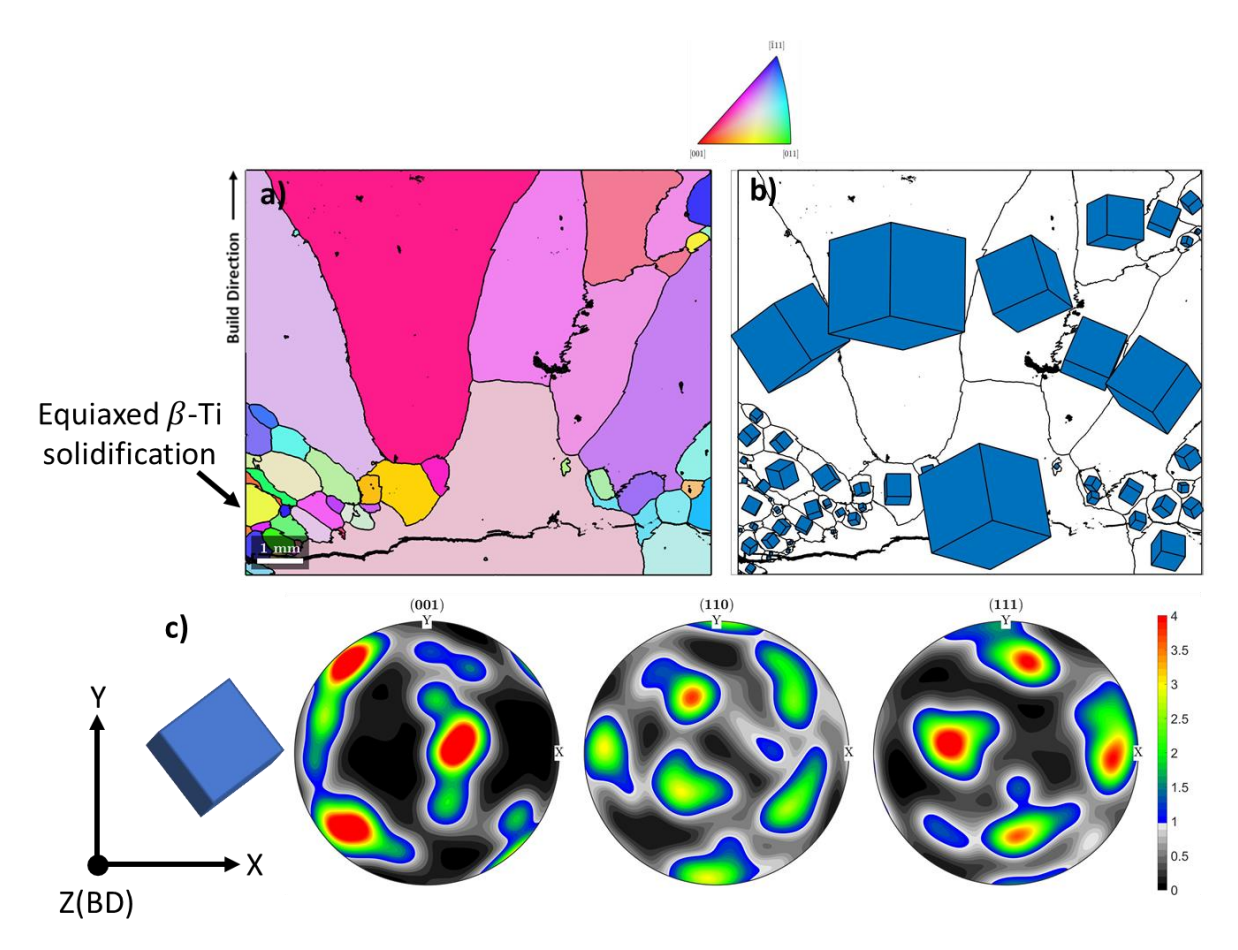


Figure 8: a)  $\beta$ -Ti IPF map illustrating equiaxed and columnar  $\beta$ -Ti grains with a stronger preference for the  $(001)_{\beta}$  poles parallel to the build direction. The fanning out of the columnar grains is indicative of a single-pass weld microstructure, formations normally observed at the beginning of an AM build. b) Crystal map of reconstructed  $\beta$ -Ti demonstrating the different alignments of the equiaxed and columnar grains. c) Reconstructed EBSD  $\beta$ -Ti pole figures demonstrating a strong alignment of a rotated cube texture around the build direction. The alignment of the  $(110)_{\beta}$  poles aligns well with the  $(0002)_{\alpha}$  poles, indicating the Burgers OR was followed here. More on this can be seen in Figure A 1. Note the crystal map and pole figures represent the same data but in different orientations.

Backscatter SEM inspection of the cracked area confirms the findings first shown in the  $\beta$ -Ti reconstructions. The crack started from the outer diameter (Figure 9a) and propagated through the equiaxed parent grains into one large interior  $\beta$ -Ti grain. Curiously, the crack bifurcated through parent  $\beta$ -Ti grains and colony structures and not along parent grain boundaries (Figure 9b). This suggests a significant stress forced this crack to propagate, considering the crack bypassed the easier-to-fracture parent grain boundaries outlined with  $\alpha$ -Ti. Secondary cracks also originating at the outer build diameter joined the main fracture  $\sim 750~\mu m$  interior to the build. The crack continued to propagate across colony structures with adjacent crack initiations (Figure 9c) previously seen in other DED builds [48], until stopping at the final  $\beta$ -Ti grain in the specimen width. This suggests the crack only propagated when the microstructure was dominated by  $\alpha$ -Ti and not at higher temperatures when in the  $\beta$ -Ti phase field. Whatever caused the formation and

propagation of this crack *nearly fractured* the entire build volume in two, stopping only 500  $\mu$ m from the inner diameter.

Figure 9d illustrates a higher magnification of the area outlined in red in Figure 9c. Interestingly, here the crack tip propagates along  $\beta$ -Ti interfaces between adjacent regions of  $\alpha$ -Ti. It is suspected this is a different crack propagation method than that which fractured the outer diameter region, considering the crack path observed in Figure 9b. The actual crack path in these areas was too small to be visible using SEM, but curvature at the ends of parallel crack lengths indicate connection of each cracked region. This again confirms the cracking occurred after the colony structure had been established.

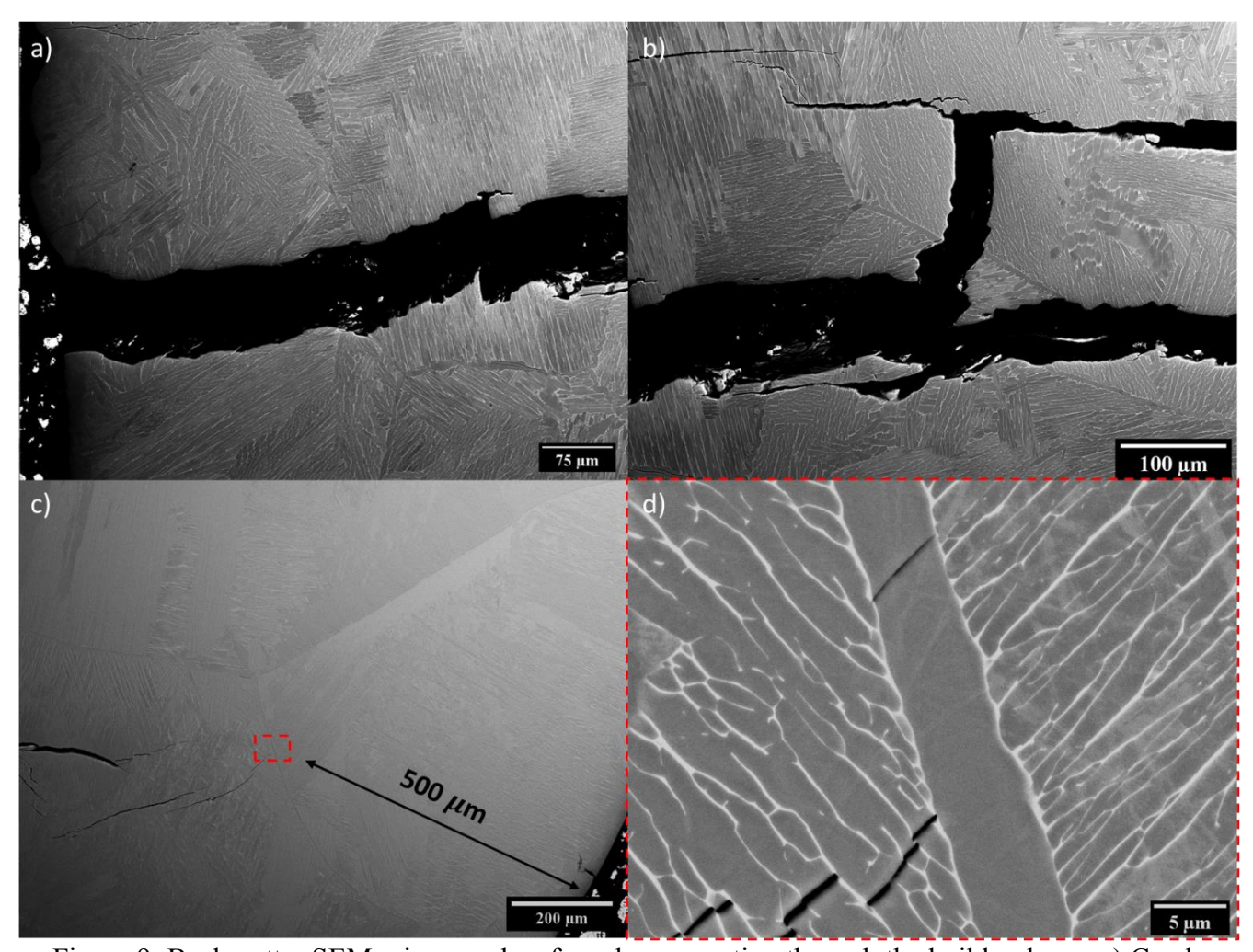


Figure 9: Backscatter SEM micrographs of crack propagation through the build volume. a) Crack initiation on the outer diameter of the build. b) Crack bifurcation through parent  $\beta$ -Ti grain boundaries, grain boundary  $\alpha$ -Ti, and through  $\alpha + \beta$  colonies. Secondary cracks are observed joining the primary crack. c) Micrograph illustrating crack bifurcations near the crack tip and how close fracture propagation was to cleaving the build geometry in two. d) Higher magnification image of the region in c) outlined in red. Here the crack tip propagated along  $\beta$ -Ti interfaces between  $\alpha$ -Ti at scales unobservable with SEM and terminated after crossing into the last  $\beta$ -Ti grain in the specimen width.

Finer inspection of the cracked region was completed with EBSD to analyze the relationship between microstructure and crack propagation (Figure 10a). The cause of the crack propagation after solidification and the solid state transformation was attributed to Type I residual thermal stresses given previous research in this area [49]. Previous work also demonstrated crack propagation in Ti-6Al-4V solid state microstructures is sensitive to the Schmid factors for both prismatic and basal slip systems in  $\alpha$ -Ti [48]. Thus, a Schmid factor calculation was completed for every  $\alpha$ -Ti orientation in the cracked region. This calculation assumed the thermal stress was aligned parallel to the build direction, as shown in Figure 10. The build direction was selected as an approximation for the residual thermal stress vector considering how a large thermal gradient exists between the active deposition surface and the solidified material below. The exact magnitude of residual stress causing this crack propagation is unknown, and an opportunity area for future modelling research. However, this value was not needed to determine Schmid factors, which are only orientation dependent.

The Schmid factor calculation in Figure 10b and Figure 10c determined the crack propagated through  $\alpha + \beta$  colonies with high Schmid factors for both the prismatic and basal slip systems. Colonies colored yellow exhibited high Schmid factors for the corresponding slip system, while blue exhibited low Schmid factors. Crack propagation continued through adjacent colonies as long as the adjacent colony had a high Schmid factor for one of the two slip systems. The active slip system often alternated between neighboring colonies. Near the inner diameter the crack began to bifurcate internally to a colony with moderate-to-low Schmid factors for both primary slip systems (red outlined region in Figure 10b and Figure 10c). This demonstrates how the lack of an accommodating slip system will frustrate crack propagation in DED Ti-6Al-4V, and confirms the relationship between favorability for crack propagation and Schmid factors. This frustrated crack propagation is similar to the crack behavior observed in Figure 9c.

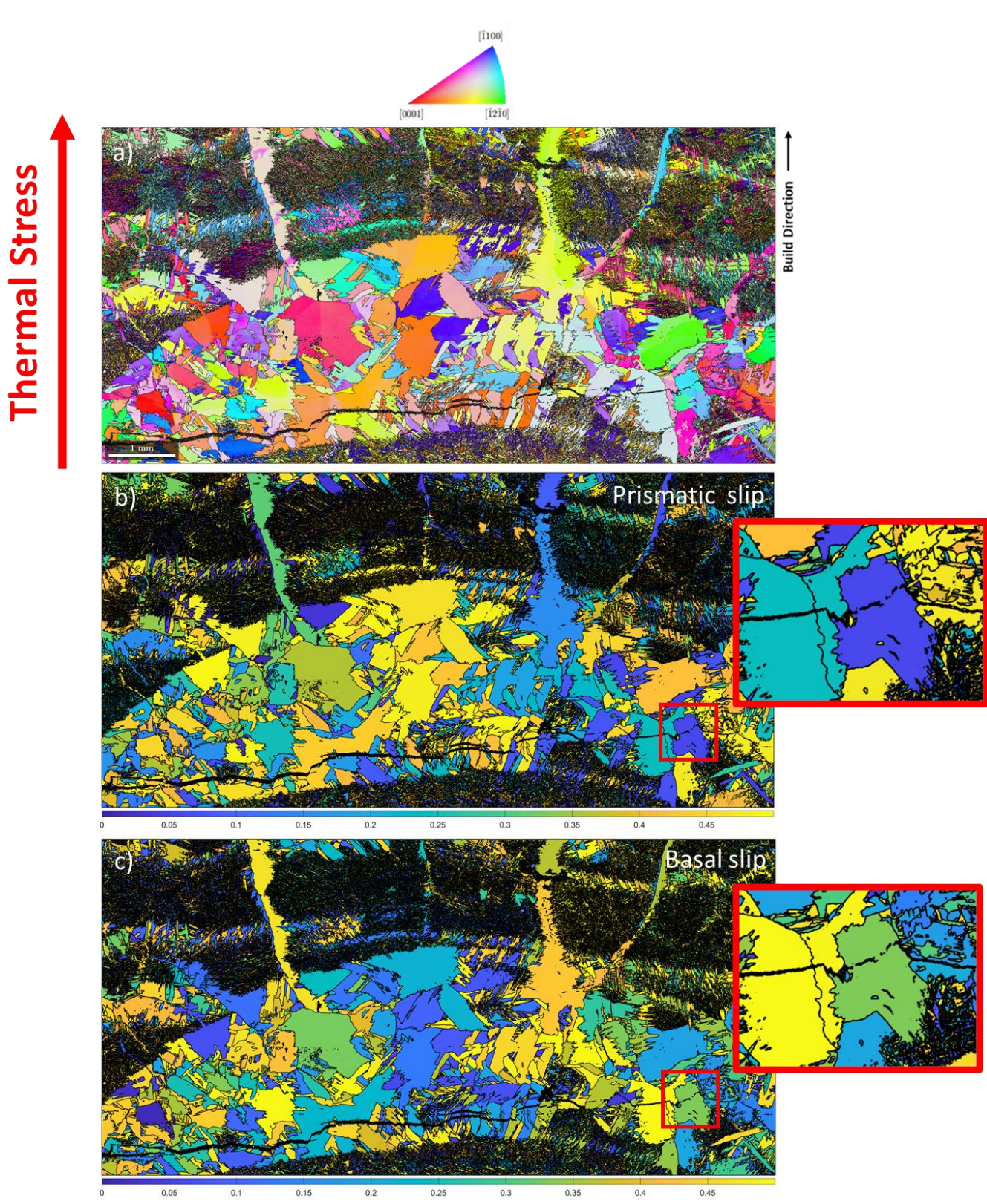


Figure 10: a)  $\alpha$ -Ti EBSD IPF map of the fractured region illustrating a concentration of uniquely oriented  $\alpha + \beta$  colonies.  $\beta$ -Ti was not included in this map. All orientations colored with respect to the build direction. b) and c) Schmid factor map for the prismatic and basal slip systems

(respectively) of each  $\alpha$ -Ti orientation. Schmid factors were calculated assuming a thermal stress parallel to the build direction. The region outlined in red identifies a colony where crack bifurcation was prominent due to the lack of a favorably oriented slip system. Crack propagation occurred through adjacent colonies with the highest Schmid factors of either basal or prismatic slip. The scale of the thermal stress arrow does not indicate the degree of stress applied, only the direction used for calculation.

# 3.2.3 100-130 mm Build Height

EBSD of the top 30 mm of build height was completed to further explore the findings observed at lower locations. Figure 11a illustrates an 11 x 8 mm  $\alpha$ -Ti IPF map centered at  $\sim$  115 mm. The microstructure here predominantly consists of the previously described four layered morphologies, but regions of singular orientations again indicate the localized presence of large  $\alpha + \beta$  colonies like before. Amongst the large colony regions, the  $(01\bar{1}2)_{\alpha}$  poles are preferentially aligned with the build direction here (pink coloration in Figure 11a). This reinforces texturing of the  $(01\bar{1}2)_{\alpha}$  poles, indicating diffusional microstructures [10]. Such texturing was not observed in the crack regions in Figure 10. KAM values also illustrate where colony microstructures and grain boundary  $\alpha$ -Ti are favored over the basketweave morphology as done elsewhere in the build (Figure 4c).

Surface cracks were captured propagating through colony microstructures and potentially a weak  $\alpha$ -casing on the outer diameter of the build (Figure 11b). These cracks are of a similar character to those observed in Figure 9 but much shorter. Figure 11c illustrates the  $\alpha$ -Ti pole figures for the surveyed area with a considerably higher intensity 12 variant texture than previously observed (maximum  $\sim 7.5$  m.r.d.). The concentration of  $\alpha$ -Ti orientations to eight primary points in the  $(0002)_{\alpha}$  pole figure corresponds to eight of the twelve variants possible from a prior  $\beta$ -Ti grain. As these orientations dominate the texture, it stands to reason only 2-3  $\beta$ -Ti grains are likely present in the surveyed area. This is visualized in Figure A 2. Some low intensity regions indicative of unique  $\alpha$ -Ti orientations do appear in the  $(0002)_{\alpha}$  pole figure. This suggests the presence of moderately sized  $\beta$ -Ti grains with different as-solidified orientations or significant enough contributions from large  $\alpha + \beta$  orientations.

A texturing of both the  $(01\overline{1}2)_{\alpha}$  and  $(11\overline{2}0)_{\alpha}$  poles is present in Figure 11c, with the latter exhibiting slightly higher intensity. This is in agreement with previous indications that preferential alignment of the  $(11\overline{2}0)_{\alpha}$  poles or the presence of a  $\{11\overline{2}0\}_{\alpha}$  fiber texture parallel to the build direction is indicative of greater fractions of faster cooling rate solid state microstructures (e.g., basketweave) [10,15,16]. No clear fiber texture is present for either the  $(01\overline{1}2)_{\alpha}$  and  $(11\overline{2}0)_{\alpha}$  pole figures, a finding likely due to the reduced number of  $\beta$ -Ti grains in this area. This is further discussed in Section 4.3.2 Texture Markers for Microstructural Condition.

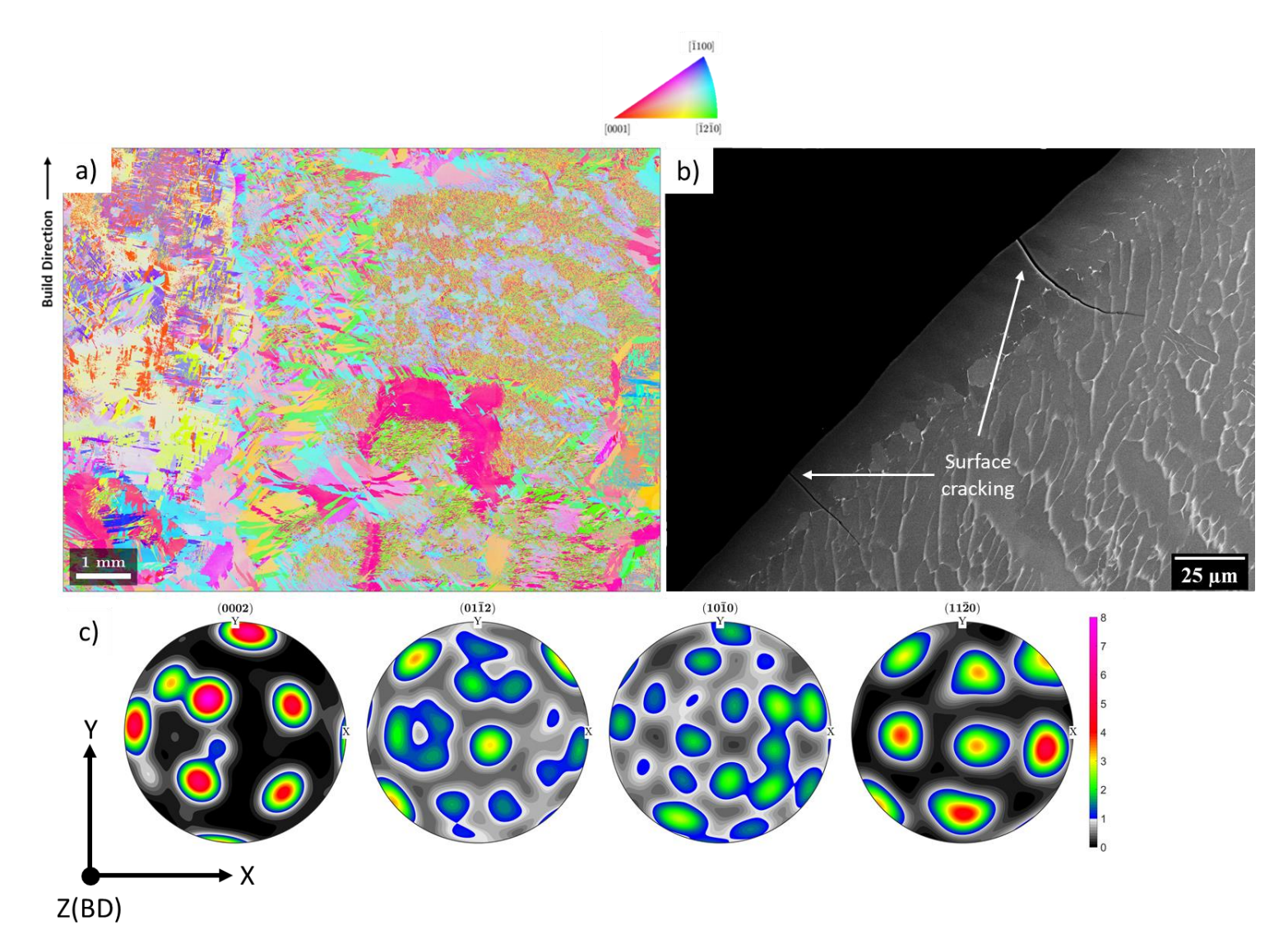


Figure 11: a)  $\alpha$ -Ti IPF map of  $\sim$  115 mm in build height. The presence of a layered microstructure is apparent, but so are localized regions of  $\alpha + \beta$  colonies with  $(01\overline{1}2)_{\alpha}$  along the build direction. b) Backscatter SEM micrograph of surface cracks originating from the build's outer diameter. These cracks traverse through large colony formations the same way cracking occurred in Figure 9, but have not propagated into the build interior. A dark layer ( $\sim$  10  $\mu$ m in thickness) at the build edge suggests the presence of a potentially embrittled  $\alpha$ -casing layer. c)  $\alpha$ -Ti pole figures illustrating an increased 12 variant  $\alpha$ -Ti texture from  $\beta$ -Ti grains with a rotated cube texture along the build direction. The appearance of *only* these variants suggest *only* one or two large  $\beta$ -Ti grains were present with the same orientation in the surveyed area.

 $\beta$ -Ti reconstruction of this region confirms the presence of one large  $\beta$ -Ti grain constituting  $\sim$  70 % of the specimen width at this location (Figure 12a). Other smaller parent grains are included in the scanned area, but have different orientations than the larger grain and are washed out in calculating texture (Figure 12b and c). The large  $\beta$ -Ti grain exhibits the expected rotated cube texture close to the build direction, considering the 12 variant texture observed previously. Curiously moderate KAM values are observed throughout the reconstructed microstructure,

potentially hinting at misorientations internal to the large  $\beta$ -Ti grains formed with the addition of subsequent layers (Figure 6c).

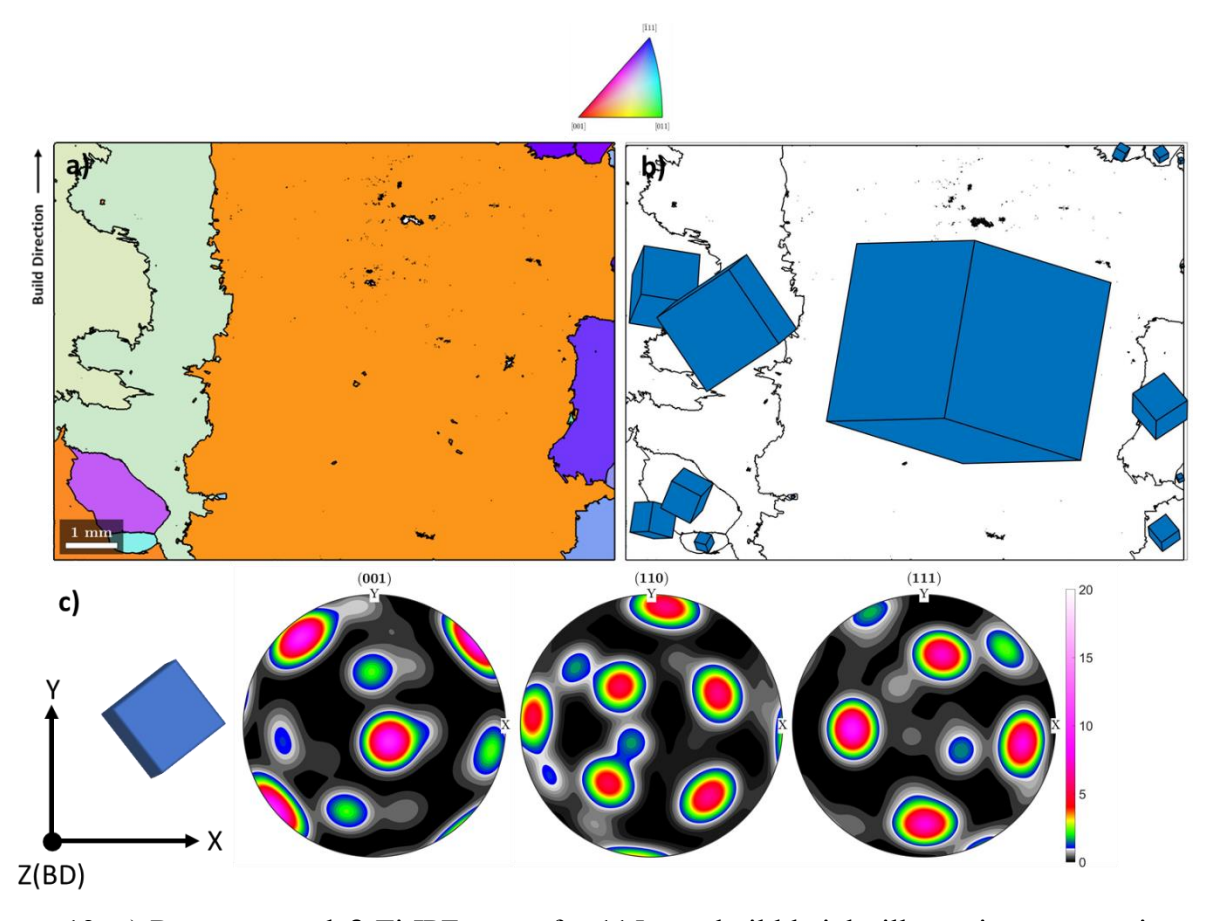


Figure 12: a) Reconstructed  $\beta$ -Ti IPF map of  $\sim$  115 mm build height illustrating one centimeter wide  $\beta$ -Ti grain. b) Crystal map of the reconstructed  $\beta$ -Ti crystals. The largest parent grain illustrates  $(001)_{\beta}$  texture just off the build direction; due to its size it washes out the textures originating from the other smaller grains in statistical considerations calculating texture. c)  $\beta$ -Ti pole figures illustrating the same data represented in b) but in accordance to the specimen reference frame. The predominant rotated cube  $\beta$ -Ti texture is also represented by the accompanying cube in c).

# 3.3 Neutron Diffraction

 $\alpha$ -Ti neutron diffraction returned similar textures to those seen in EBSD, also capturing the 12 variant texture throughout the build height. This validated the effectively 2D orientation data collected via EBSD as representative of the actual 3D microstructure. An example set comparing the regions analyzed in Figure 7 and Figure 11 are included in Figure 13. At  $\sim$  40 and 115 mm build heights, neutron diffraction and EBSD returned almost exactly the same  $\alpha$ -Ti textures. This confirms the validity of the EBSD data and reference frames presented previously. Though pole figures for the same regions reported the same texture intensities, neutron diffraction texture data appears rotated  $\sim$  20° around the build direction from that measured in EBSD. This will be discussed further in Section 4.2.2 Neutron Diffraction.

# 115 mm Build Height

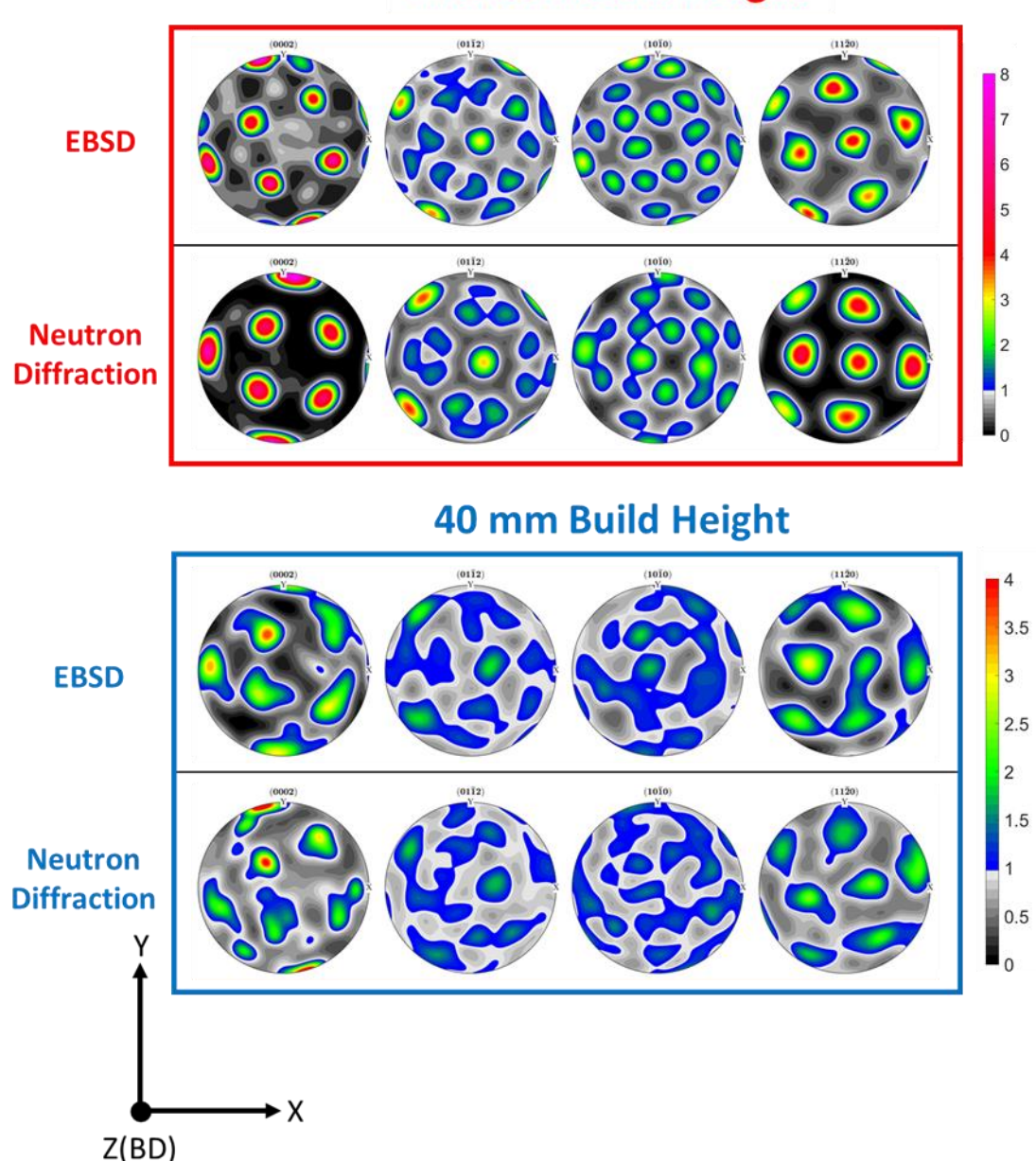


Figure 13:  $\alpha$ -Ti pole figures comparing textures measured via EBSD and neutron diffraction for 115 mm and 40 mm build heights. Note the different color scales used for both sets of pole figures in reflection of the change in  $\beta$ -Ti grain size.

Neutron diffraction of the build's outer rim was also completed. Instead of being built with a linear traversal in the XY-plane of the build reference frame, the outer rim was produced with linear traversals along the XZ-plane. Here, material was deposited up and down the Z-axis. Thus, the solidification direction and texture likely changed compared to the previously analyzed build volume. Such an environment also gives further insight into the previously described crystallographic texture markers. The Z-axis is not equivalent to the build direction for this material. Rather, the Y-axis can be thought of as the build direction for the outer rim, while the X-

axis still acts as the travel direction. All pole figures will still be reported in the reference frame outlined in Figure 1 however.

The bottom of the outer rim demonstrated different  $\alpha$ -Ti textures than that observed anywhere else in the build (Figure 14). Both a  $\{01\bar{1}2\}_{\alpha}$  and  $\{11\bar{2}0\}_{\alpha}$  fiber texture are present with comparable intensities, but oriented normal to the Z-axis (90° off the center of the pole figure). The presence of these textures suggests a colony and basketweave microstructure near where the outer rim was first deposited [10]. Since previous work showed these textures and indicated the direction of solidification [10], it can be assumed the concentrated  $(01\bar{1}2)_{\alpha}$  and  $(11\bar{2}0)_{\alpha}$  orientations southwest of the build direction correlate to the  $\beta$ -Ti solidification direction. At a ~ 30° offset from the Y-axis, this is effectively the same tilted solidification observed in Figure 5. The only difference here is that the ~ 30° tilt in the outer rim is in the XY-plane, and not the XZ- or YZ-planes. The presence of these textures as fibers also means  $\beta$ -Ti was able to rotate freely around the solidification direction distribute  $\alpha$ -Ti variants in a circular fashion. This can be observed most clearly in the  $(0002)_{\alpha}$  pole figure and discussed more in Section 4.3.2 Texture Markers for Microstructural Condition.

At the top of the outer rim,  $\alpha$ -Ti takes on textures similar to those at higher build heights. This shows the  $\beta$ -Ti transitioned from solidifying normal to the Z-axis to solidifying parallel to the Z-axis over the height of the outer rim. The lack of any fibers demonstrates larger  $\beta$ -Ti grains are present at the top of the outer rim, as shown in Figure 12. Meanwhile, the increased texture of the  $(11\overline{2}0)_{\alpha}$  poles over the  $(01\overline{1}2)_{\alpha}$  predicts the formation of primarily a basketweave microstructure and a return to typical DED microstructures.

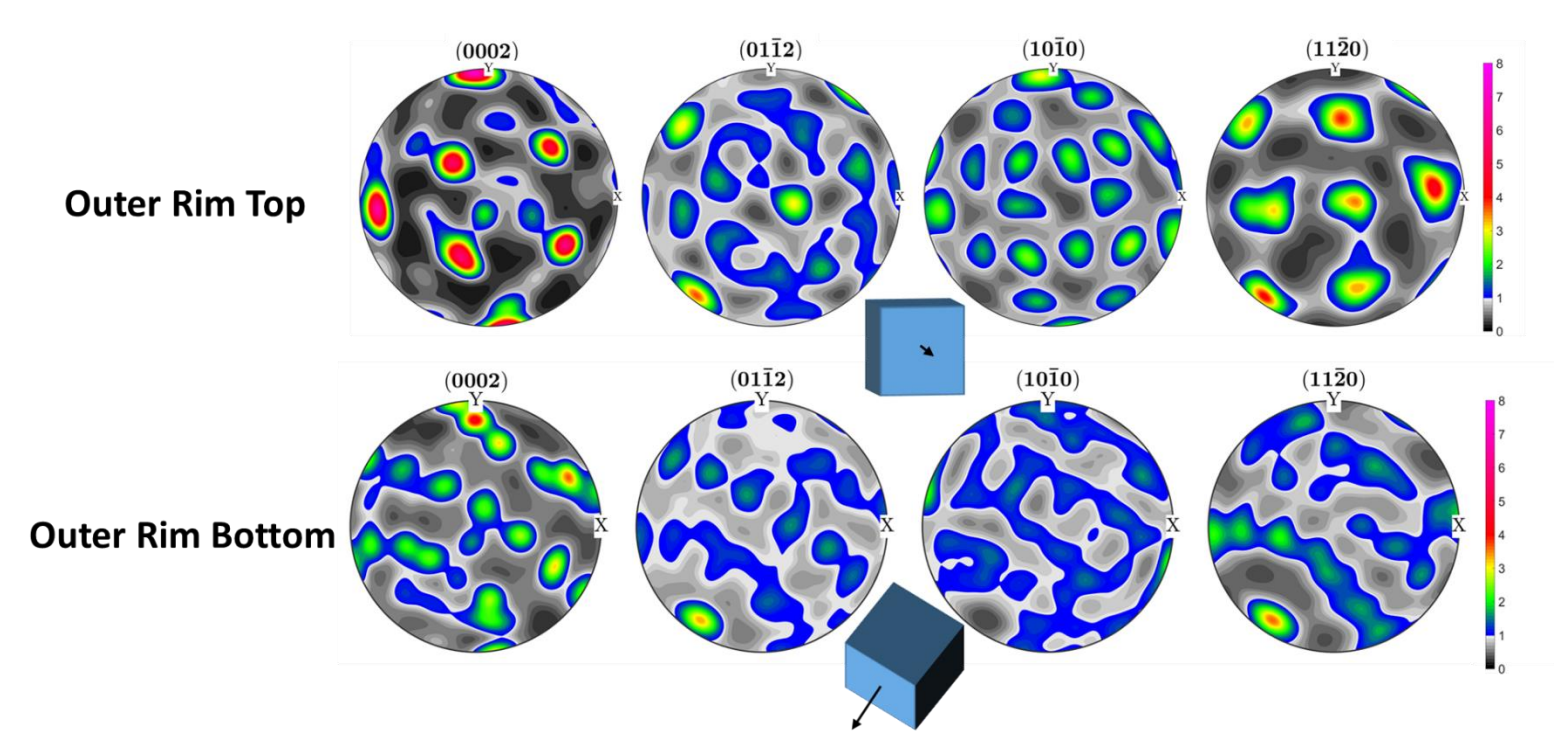


Figure 14:  $\alpha$ -Ti pole figures from neutron diffraction of the build's outer rim. A shift in solidification direction was observed from the bottom to the top of the outer rim. The solidification direction is indicated by the black arrow on the representative cube.  $\beta$ -Ti solidified normal to the Z-axis (off previously deposited material) at the beginning of the outer rim, able to freely rotate around the solidification direction and produce  $\alpha$ -Ti fibers. At the top,  $\beta$ -Ti was solidifying along the build direction with similar  $\alpha$ -Ti textures to other locations in the build.

# 4. Discussion

#### 4.1 Microstructure

#### 4.1.1 Layered Microstructures

The layered microstructure observed for the morphologies in Figure 2a-d is thought to originate from differences in solid state cooling rates in layers below the current deposition [43]. Immediately after deposition, material just below the deposited layer will be heated above the  $\beta$ -Ti transus, completely removing any established  $\alpha + \beta$  microstructures. Following the application of the most recent layer, this material will rapidly cool into a fine basketweave morphology (dark green region in Figure 15) as heat is extracted through the build volume into the base plate. The same logic would predict the freshly deposited material should transform into a martensitic or fine basketweave structure with rapid cooling. However, the most recently deposited material transforms into a fine colony microstructure instead (Figure 15). Kelly and Kampe also observed this and theorized such microstructures were due to non-equilibrium conditions changing the transformation pathway for freshly deposited material [43].

Material multiple layers below the deposition layer will be heated higher into the  $\alpha + \beta$  regime and subsequently cooled at slower rates than material higher in the above layers after the most

recent deposition (yellow in Figure 15). Material closer to the build surface will be heated more than material in previous layers, creating a thermal gradient. Material furthest away from the deposition will minimally be heated and retain a fine basketweave morphology after cooling. Material just above this region will be subjected to higher temperatures, and produce a slight coarsening of the basketweave  $\alpha$ -Ti and an increase in  $\beta$ -Ti phase fraction. Above this point, the local microstructure is heated closer to the  $\beta$ -Ti regime and undergoes significant transformation of the initial fine basketweave morphology. Upon cooling, the local conditions produce the elongated "bowtie"  $\alpha + \beta$  colonies. The top layer of material will be subject to heating *just* below the  $\beta$ -Ti transus, and thus undergo significant transformation with the growth of more equilibrium  $\beta$ -Ti. This layer will also be subject to the fastest cooling of any of the layered tiers, and upon cooling will transform into high-aspect ratio plate colonies akin to Widmanstätten plates in ferrous alloys and meteorites.

After this complex series of thermal interactions, the layered microstructure will be unaltered and retained in the build volume. Heat input from new depositions will insufficiently alter the four previously described microstructures, locking in the tiered morphologies observed here. Some variation at the build start and build finish may be present as these thermal conditions may not be fully achieved. Previous phase field modelling supports such microstructural evolution, though more complex analysis is required to account for changes in build parameters and energy sources [32].

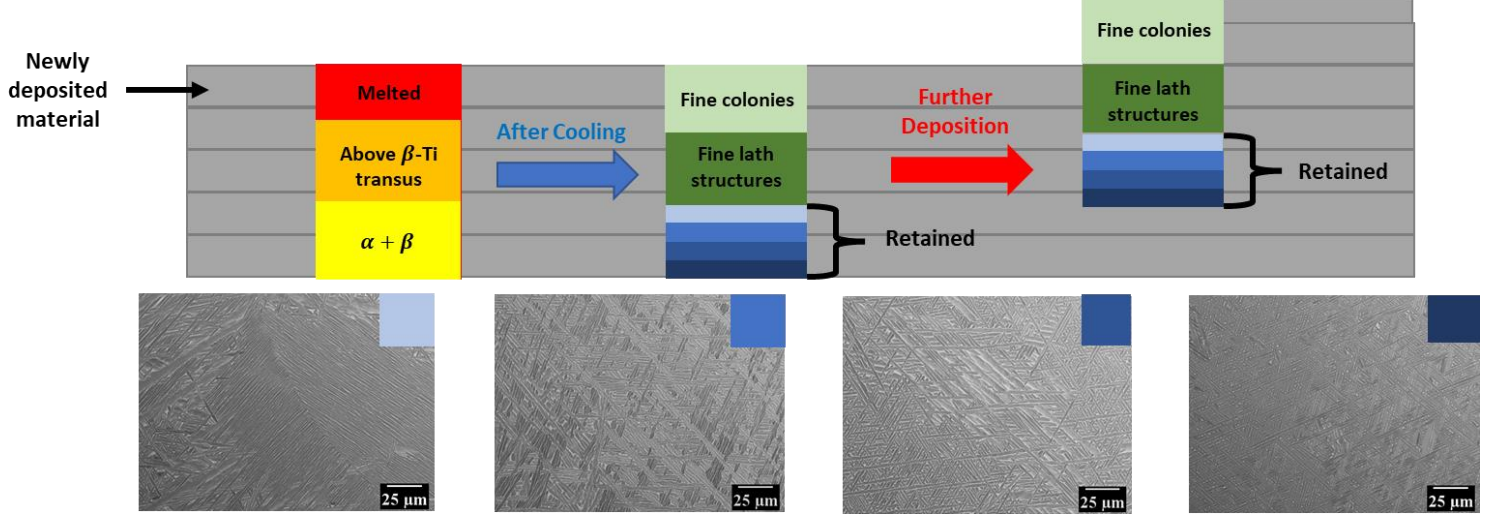


Figure 15: Illustration depicting the formation of the layered microstructures predominantly observed in the DED Ti-6Al-4V specimens. Material multiple layers below the deposition layer will be heated higher into the  $\alpha + \beta$  regime and undergo different solid state cooling rates. This produces the layered microstructure observed predominantly through the material.

# 4.1.2 Coarse Colony Microstructures

Coarse colony structures greater than 100  $\mu$ m in length were observed at the edges of the build volume (Figure 2e) and in local regions within the layered microstructure previously described (Figure 2f). Such morphologies are evidence of considerably slow and sustained cooling rates. These conditions are atypical considering the presence of basketweave morphologies throughout the build, indicative of faster solid state cooling rates than those for colony formation.

Colonies interior to the build were observed predominantly near regions where smaller  $\beta$ -Ti grains appeared to be forming. Such a correlation was not accidental, as it was later discovered pauses of the build process had occurred for unknown timespans. Though this complicates the thermal history of the DED microstructure, such conditions are more in line with realistic AM operations where such scenarios are possible.

Traditional  $\alpha + \beta$  colonies are formed via atomic diffusion, requiring slower cooling rates than the aforementioned basketweave morphologies. Such conditions would be present in the most recently deposited layer, where large heat inputs sustain higher temperatures for diffusion to occur. However, large colonies are not maintained upon further deposition as the next deposition heats this microstructure into the  $\beta$ -Ti regime. This fully removes the colony microstructure, and instead begins the evolution illustrated in Figure 15.

The only way for colonies to be maintained upon further deposition is with insufficient heat input to reach the  $\beta$ -Ti regime. Assuming build parameters are not changed, this can be achieved by a pause in the build process allowing for some or all residual heat to dissipate. This lowers the average build temperature potentially as far as ambient conditions, depending on duration. Consequently, restarting the deposition process may not raise the temperature of previously deposited material above the  $\beta$ -Ti transus. Material deposited before the pause occurred is reheated above the  $\beta$ -Ti transus due to the heat accumulated from continuous deposition. With the build pause however, this thermal saturation is removed and new deposition is prevented from retransforming solid state microstructures. Effectively, the fine colony microstructure does not transform into fine lath structures and is retained, skipping the second phase of microstructural evolution in Figure 15. This leftover colony microstructure may be heated sufficiently to enable atomic diffusion and coarsen the existing colonies, but complete transformation does not happen. This gives rise to the colony microstructures observed throughout the EBSD surveyed areas, and also likely at the bottom of the outer rim as demonstrated by the textures in Figure 14. This is additionally supported by phase field modelling, though further work is needed to fully account for the rapid reheating processes associated with AM build processes [32].

Such a thermal environment would also mean heat would be extracted faster during solidification. Heat would be pulled faster out of the liquid into the now cooled build volume, and thus increase solidification velocity. This in turn favors the equiaxed solidification morphology and explains the presence of equiaxed  $\beta$ -Ti grains near or slightly above large interior  $\alpha + \beta$  colonies. The large size of these equiaxed grains again indicates low  $G \times V$  solidification values, in line with the scale of the columnar  $\beta$ -Ti compared to other build processes [8,10,14,27] and phase field modelling of Ti-6Al-4V during solidification [32,44–47].

It is unknown whether shielding gas was still applied to the active surface during the build pause. If not, it could be possible for oxygen to contaminate the active surface and additionally favor equiaxed solidification given the Q-value for this element [50]. No oxygen partitioning or oxide formations were found during exploratory EDS, but simulations and wavelength dispersive spectroscopy (WDS) could inform the feasibility of such conditions further. Excess oxygen at the active surface from the build pause could also artificially stabilize  $\alpha$ -Ti in the form of colonies, assisting in retaining this microstructural morphology in the solid state. An example EDS map was completed on an equiaxed  $\beta$ -Ti region, and is included in Figure A 4 showing no obvious partitioning or oxide formation internal to the build.

Just above these equiaxed  $\beta$ -Ti grains appear fanned out columnar grains similar to those seen in single-pass welds. Such angular tilt of the  $\beta$ -Ti is only seen near build pauses considering the unique thermal conditions previously described. With the build geometry containing very little heat after the build pause, thermal gradients are less aligned with the build direction and more sensitive to the position of the incident heat source. Thus, as the deposition travels in the XY-plane,  $\beta$ -Ti will follow the traversal of the heat source and fan out across the specimen width along the Y-axis. Grains near the edge of the build volume will have their  $(001)_{\beta}$  solidification direction tilted  $\sim 15\text{-}25^{\circ}$  off the build direction, while grains near the center of the build will maintain a  $(001)_{\beta}$  along the build direction and slightly towards the travel direction. After further depositions and no further build pauses, the central grain with the  $(001)_{\beta}$  poles aligned closer to the build direction will win out and outcompete those with an unfavorable crystallographic orientation of the  $(001)_{\beta}$  poles. This previous logic explains the microstructural evolution seen throughout the reconstructed  $\beta$ -Ti map seen in Figure 8.

Large colonies at the build edges also formed due to slower solid state cooling rates but from a different mechanism. Traversing in the XY-plane as described in Figure 1b should give roughly comparable thermal conditions at all points in the design geometry. However, video of the deposition process (Figure A 5) demonstrates this is not the case. To avoid edge sagging of the inner or outer diameters, the TIG torch did not traverse completely across the specimen width. Rather, the TIG torch has its travel direction flipped before centering on the build edge. This applies a partial heating of the edge material analogous to that seen after the build restarts. The edge material is thus theorized to be heated well below the  $\beta$ -Ti transus, and colony microstructures produced from previous depositions can be retained. This partial heating could also sufficiently alter the solidification conditions during new deposition and incentivize equiaxed  $\beta$ -Ti solidification. Finer equiaxed  $\beta$ -Ti grains were only seen at the edge of the reconstruction in Figure 8a, not at the center. The incomplete heating captured in Figure A 5 could also explain this. Further modelling and experimentation would be required to confirm these findings, though previous phase field modelling of solidification and solid state conditions suggests such evolution is realistic [32]. Oxygen contamination could also lead to increased favorability of equiaxed solidification and colony microstructures at the build edges, but this is expected to have significantly less effect.

Regardless, this investigation has shown specific tailoring of the DED build parameters can enable complex microstructural control from simple input changes. Though this is not a major revelation considering the vast research ongoing into microstructural control in AM, the previous section demonstrates an unusual way to create a "colony shell" for a DED build process with Ti-6Al-4V. Fracture resistant and fracture prone core regions were also produced using the same logic, showcasing the thermal considerations required for the tailored implementation of DED for microstructural control.

#### 4.2 Crystallographic Texture

#### 4.2.1 EBSD

The EBSD maps included in this work are larger in area than the cross-sections of small LBPB and PBF-EB parts, often by orders of magnitude. Such large areas were surveyed to capture a sufficient number of orientations to be representative of the build. When represented in pole figures

however, these textures appear artificially sharpened, akin to those observed with smaller EBSD area scans internal to one parent grain. This behavior was attributed to the scale of  $\beta$ -Ti grains in this DED build. Most AM builds will have dozens if not hundreds of  $\beta$ -Ti grains constituting a part's width, while here the build is at times only two-to-three  $\beta$ -Ti grains wide. The material effectively solidifies as a single  $\beta$ -Ti crystal, meaning only the  $\alpha$ -Ti orientations from the enormous parent grain at  $\sim$  115 mm build height will significantly contribute to the part's texture and properties. Thus, these textures are actually representative of the *full* material and demonstrate significant anisotropy could be achieved from both the product and parent phase orientations. Future investigations on this topic are planned.

Despite more  $\beta$ -Ti grains being present in the surveyed microstructure at lower build heights,  $\alpha$ -Ti continually exhibited the *12 variant texture* exhibited in Figure A 2. This was attributed to the larger  $\beta$ -Ti grains in these regions having a sufficiently common  $(001)_{\beta}$  solidification direction and limited rotational freedom. Thus, after the  $\beta \to \alpha$  transformation the same orientations emerge, albeit with different intensities. The rotation of the solidification direction from towards the travel direction (X-axis) to the build direction (Z-axis) occurs as the build becomes thermally saturated and less sensitive to the most recent thermal input. Overall thermal gradients track closer to the build direction at higher build heights, and thus the  $(001)_{\beta}$  poles correspondingly shift.

The intensity of the 12 variant  $\alpha$ -Ti textures also increases with increasing build height. As  $\beta$ -Ti grain size goes up, less material in the build width has a unique parent phase orientation. After the  $\beta \to \alpha$  transformation, assuming no variant selection, the largest parent grain will transform to all of the same 12 variants and dominate the product phase orientations. Though other  $\alpha$ -Ti orientations exist over centimeters of area, these are washed out in the statistical calculation of ODF's and pole figures. Thus, as the average  $\beta$ -Ti grain size goes up with build height, so too does the average  $\alpha$ -Ti texture and potential anisotropy. Reconstructed  $\beta$ -Ti texture also scales with the  $\beta$ -Ti grain size in this build, demonstrating a new way to quickly evaluate the solidification condition of an AM build from  $\alpha$ -Ti texture.

# 4.2.2 Neutron Diffraction

The relative rotations of the EBSD and neutron diffraction pole figures in Figure 13 were thought to originate from different angular positions of  $\beta$ -Ti grains in the sister sample sent for neutron diffraction. Each sister specimen sat to the left of the EBSD specimens in the build reference frame (11:30 am vs 12:30 pm on a clock face). Considering the right specimen demonstrated a preference for solidification with a 5-10° clockwise rotation around the build direction, it stands to reason a 5-10° counterclockwise rotation could also exist for the sister specimens on the left. This should produce a mirror image of the same orientations around the Y-axis. Thus, the position of each sample would result in slightly different rotations of the same textures and produce a rotation relative to one another. This accounts for the differences observed in Figure 13.

Considering neutron diffraction and EBSD complement each other in all respects, no further investigation with neutron diffraction was completed for the four primary specimens. EBSD texture measurements can be established as representative of the 3D microstructure at the scales analyzed.

The change in  $\alpha$ -Ti orientations along the outer rim's height is indicative of not just microstructural evolution in the solid state and  $\beta$ -Ti grain size, but also local solidification conditions. Previous

work has shown finer  $\beta$ -Ti grains have the ability to rotate around a solidification direction in AM of Ti-6Al-4V [8,10]. This also influences the solid state texture, producing  $\{11\overline{2}0\}_{\alpha}$  and  $\{01\overline{1}2\}_{\alpha}$  fibers for the  $\alpha$ -Ti and a  $\{001\}_{\beta}$  fiber for  $\beta$ -Ti along the solidification direction. Such  $\alpha$ -Ti fibers occur by the 12 possible  $\alpha$ -Ti variants being spatially distributed around the build direction in accordance with the Burgers OR from  $\beta$ -Ti crystals rotated at times only a few degrees apart. This is discussed further in Section 4.3.2 Texture Markers for Microstructural Condition. This process may include some variant selection should only one  $\alpha$ -Ti fiber be present [10] or none if both primary fibers are observed.

Thus, it can be inferred from Figure 14 limited to no variant selection occurred in a large amount of finer  $\beta$ -Ti grains at the bottom of the outer rim. Conversely, only a few large  $\beta$ -Ti grains constituted the microstructure at the top of the outer rim with few  $\alpha$ -Ti orientations making up the  $\sim$  6x m.r.d. texture. Again, no variant selection was observed considering the presence of the eight variants expected for the upper half of the stereographic projection.

# 4.3 Relating Crystallographic Texture and Microstructure

#### 4.3.1 Crack Propagation

The near complete fracture of this build volume and evidence for additional cracking throughout the build height pose a major challenge to DED of Ti-6Al-4V. Thermal stresses were theorized to be the primary catalyst for cracking in this build. Surface roughness from the deposition of each layer was also thought to act as primary crack initiation sites, with thermal stresses putting notches in the outer diameter into a Mode 1 loading condition.

The near complete fracture of the DED build occurred *only* in a region of material where large  $\alpha + \beta$  colonies existed throughout the microstructure. Other regions where large colonies only existed at the build edges did not have nearly as much crack propagation, though some was still observed. The higher cooling rate basketweave microstructure appeared much more resilient to crack propagation than colonies.

 $\alpha + \beta$  colonies represent regions of continuous  $\alpha$ -Ti crystal in-between ribs of  $\beta$ -Ti. This local pseudo single crystal can act as an analogous super highway for rapid crack growth considering few significant barriers are present to arrest further propagation. A basketweave morphology meanwhile contains many more uniquely oriented  $\alpha$ -Ti crystals with far more barriers. This is comparable to using backroads in lieu of the highway in the present analogy. This creates a more tortuous crack path and explains why crack propagation was arrested into the build interior for regions of basketweave morphologies.

Clear evidence for the dependence of crack propagation on the alignment of the basal and prismatic slip systems was also observed. This confirms crack propagation occurred in the solid state, suggesting thermal conditions were indeed a factor in the fracture process. No such dependence should be observed if cracking occurred in the  $\beta$ -Ti regime. This is additionally supported by the crack propagating through one large  $\beta$ -Ti grain just below equiaxed grains. Crack bifurcation was also explained by low Schmid factors for both basal and prismatic slip in a few large colonies, demonstrating a useful tool for analyzing fractures from an AM build.

The drastically different fracture behavior between colony and basketweave morphologies in the DED build process demonstrates a potential mechanism for build tailoring. Failure in some applications *must* occur in specific locations, and the controlled creation of a large colony microstructure could act as this failure location. Alternatively, a large colony region could also be built to easily separate parts from build plates or other geometries. Such regions may also be useful in controllably relieving thermal stresses during AM builds in sacrificial build sections.

These findings also highlight the danger of uninformed pauses to an AM build. The change in local thermal condition can significantly alter the solid state and as-solidified microstructures. Though some beneficial solidification phenomena were observed, the solid state became more fracture prone. Again with careful management this could have been remedied (increasing dwell time for the layer after a build pause was completed) or thoughtfully implemented for unique part properties.

Due to the affinity titanium has for oxygen, crack propagation and formation could also have been caused by oxygen during the build process. Embrittlement of  $\alpha$ -Ti from excess oxygen and other interstitial pickup has been previously demonstrated in casting and AM of titanium components [51,52]. In AM, this so-called  $\alpha$ -case typically forms in open air builds of titanium alloys where the flow of shielding gas is insufficient to prevent oxygen interaction with active build surfaces. The DED build process employed here is one such example, and could exhibit  $\alpha$ -casing at the build extremities if insufficient gas flow rates occurred locally. This would produce an embrittled outer build shell, enable the easier formation of surface cracks upon application of any stress, and produce the cracking phenomenon observed throughout the build volume.

Such an embrittled outer shell was not dominant through the build volume, but is thought to be present in some locations at the build edge as shown in Figure 11. A layer of dark  $\alpha$ -Ti is present at the build edge as demonstrated by the lack of brighter  $\beta$ -Ti in this region. The ease with which surface cracks propagate through this layer suggests this portion of the microstructure is embrittled in some way. Only upon entering the  $\alpha + \beta$  region do the cracks begin to significantly change trajectory, again indicating the crack initiation site is brittle in nature. The same effect was seen throughout the build height, albeit only at the very surface of the part. This indicates insufficient shielding gas was implemented to fully prevent oxygen pickup at the build edges, leading to a partially embrittled surface and in some areas, local crack propagation. Increased oxygen content could also help favor the formation of colony microstructures or equiaxed  $\beta$ -Ti grains at the build edges as previously discussed.

As a result of this oxygen pickup, it can be stated the crack formation and propagation in this work was likely due to two factors. Residual stresses from thermal gradients caused cracks to form in a partially embrittled outer  $\alpha$ -casing shell formed by oxygen pickup. These cracks would propagate into the build interior in regions where the solid-state microstructure contained a soft  $\alpha + \beta$  colony microstructure with few barriers to crack propagation. Such microstructures are only possible from thermal conditions introduced by a build pause however, producing atypical solid state and solidification microstructures.

Oxygen may have imparted a small amount of embrittlement to such regions and altered the transformation/solidification phenomenon as previously discussed. These effects are considered much less significant than the thermal effects from the build pause however, especially considering the ductile behavior of the internal crack propagation in Figure 9 and Figure 10. The favorability

of crack propagation along the prismatic and basal slip systems may indicate the degree to which oxygen interacted with the top surface during the build pause, but further work is needed to clarify this.

It is thought the effect of oxygen pickup and the formation of  $\alpha$ -casing only affects the crack propagation at the surface of this DED build, and not the rest of this work. This is supported by the consistency of microstructural morphology, solidification grain size, slip-system and crack propagation, and orientation evolution to other works. However, it cannot be denied oxygen may have minutely influenced some aspects of microstructural evolution in nuanced ways undetectable in this work.

# 4.3.2 Texture Markers for Microstructural Condition

This work was initially started to evaluate if the presence of specific  $\alpha$ -Ti textures indicated the microstructural condition of Ti-6Al-4V during build processes other than PBF-EB [10]. More specifically, the presence of a  $\{01\overline{1}2\}_{\alpha}$  fiber texture along the solidification direction was shown to be an indicator of finer parent  $\beta$ -Ti grain sizes or of diffusional microstructures. The  $\{11\overline{2}0\}_{\alpha}$  fiber texture was also found in faster cooling, solid state microstructures. From this investigation, it was found both parent grain size and the character of the solid state microstructure appeared to give rise to these characteristic fiber textures [10].

To explain this further, take for example a singular  $\beta$ -Ti grain in an AM build. One set of  $(001)_{\beta}$  planes will be aligned with the build direction (Z-axis in this example) while the remaining four  $(001)_{\beta}$  planes can rotate freely around the build direction. Upon solidification however, these poles become fixed. This produces pole figures like that in Figure 12c. After undergoing the  $\beta \rightarrow \alpha$  transformation and assuming no variant selection, 12 different  $\alpha$ -Ti orientations will appear akin to those in Figure 11c. Lower intensity points besides the 12 variant texture will not be present in this idealized case. Regardless, this would be the final product texture for this AM build, with no fiber textures along the solidification direction present. Note in this case the solidification direction is assumed to be equivalent to the Z-axis and build direction.

In order for a fiber texture to appear in the  $\alpha$ -Ti pole figures, the  $\beta$ -Ti also has to exhibit a fiber texture prior to transformation. This would mean the idealized singular  $\beta$ -Ti grain must have its four  $(001)_{\beta}$  poles not aligned to the Z-axis be free to rotate around the solidification direction. This is crystallographically impossible, as these four  $(001)_{\beta}$  planes *must* be aligned 90° from one another given the cubic symmetry and more  $(001)_{\beta}$  planes do not exist. Thus, one grain cannot produce a fiber texture (Figure 16) around the solidification direction.

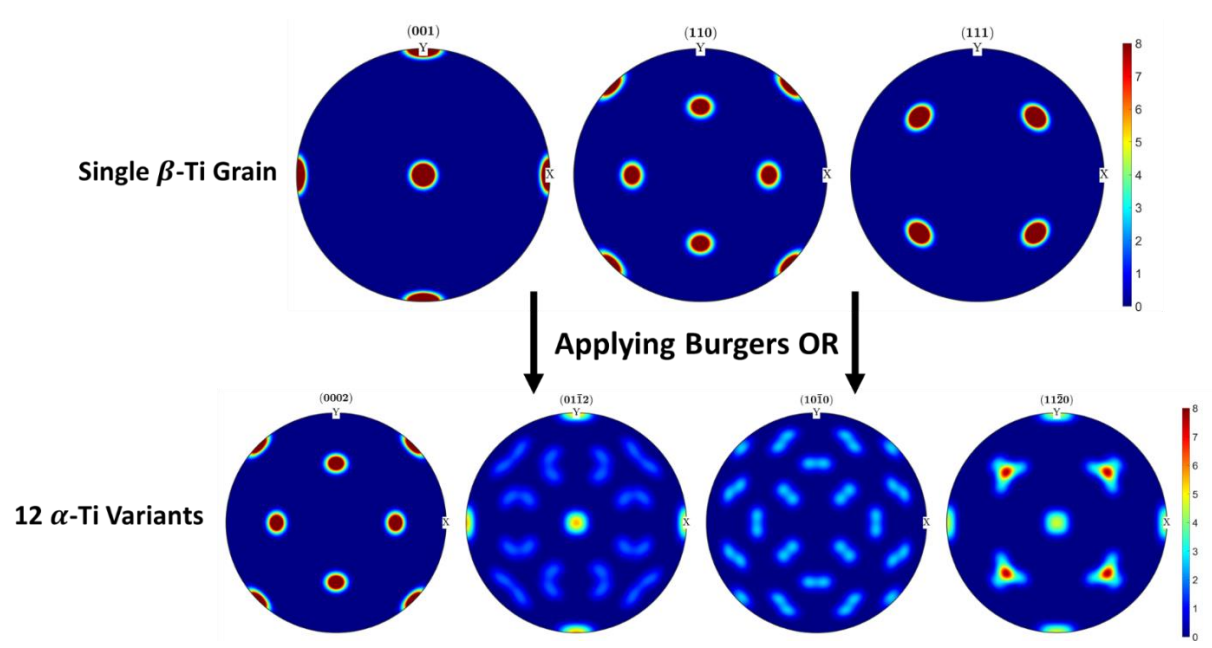


Figure 16:  $\beta$ -Ti pole figures (top) and  $\alpha$ -Ti pole figures (bottom) for a simulated  $\beta \to \alpha$  transformation. The parent  $\beta$ -Ti grain is aligned with two  $(001)_{\beta}$  poles in line with the Z-axis (solidification direction during this simulated AM build) and the remaining  $(001)_{\beta}$  poles along the Y- and X-axes. This prevents the formation of any fiber textures and restricts the  $\alpha$ -Ti orientations to the 12 variant texture calculated here. Note the  $(01\overline{1}2)_{\alpha}$  and  $(11\overline{2}0)_{\alpha}$  poles exhibit a concentration of orientations along the solidification direction. All reference frame axes are the same as those previously described for this work. Simulations completed with MTEX 5.70.

Now take a second idealized case. If  $10 \beta$ -Ti grains are present in an AM build, each of them will orient one set of  $(001)_{\beta}$  planes along the solidification direction. But, these 10 different grains will each also have four  $(001)_{\beta}$  planes that can orient themselves around the solidification direction independent of other grains. This does not break the cubic crystal symmetry as the orientation of planes in one grain will not affect the planar orientations in another.

If all these 10 grains orient their four remaining  $(001)_{\beta}$  poles around the solidification direction differently, then a circle of  $(001)_{\beta}$  poles would appear at the edge of the pole figure. The same would be true for the  $(110)_{\beta}$  and  $(111)_{\beta}$  pole figures. Following the Burgers OR, the  $(0002)_{\alpha}$  poles will transform off the  $(110)_{\beta}$  planes. If these are oriented in a circle around the solidification direction, then the  $\alpha$ -Ti will inherit the same orientations. As a result, fiber textures appear in the product microstructure around the solidification direction. If rotated 90° to the southwest, the  $\alpha$ -Ti textures observed for the beginning of the outer rim are generated (Figure 14).

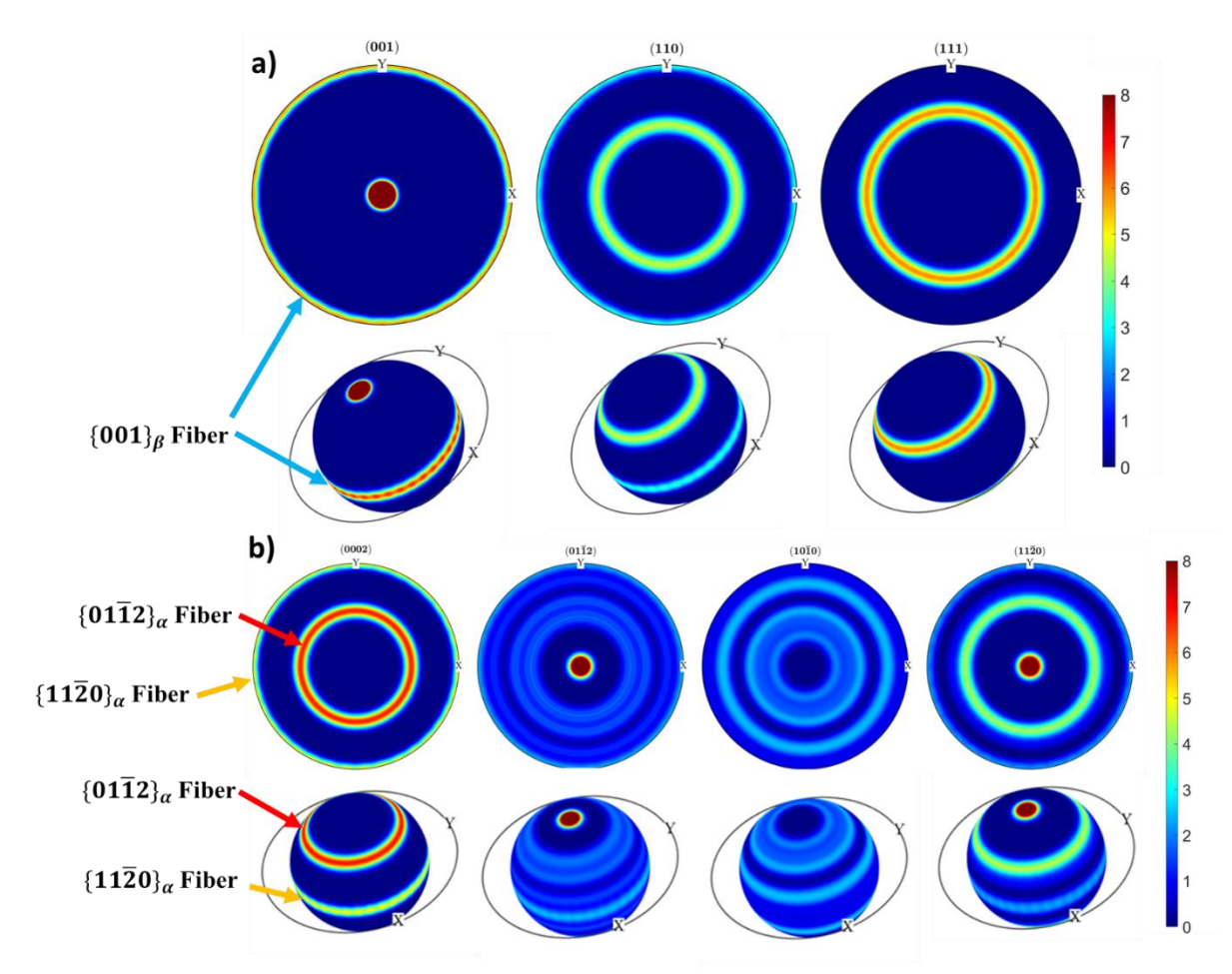


Figure 17: a) Simulated  $\beta$ -Ti pole figures for 10  $\beta$ -Ti grains oriented along the solidification direction (out of the page) but also free to rotate around the solidification direction. The top three pole figures illustrate a  $\{001\}_{\beta}$  fiber texture in 2D. The below pole figures illustrate the same orientations in 3D, more easily illustrating the  $\{001\}_{\beta}$  fiber texture along the solidification direction. b) Simulated  $\alpha$ -Ti orientations calculated from the  $\beta$ -Ti orientations in a). Again, 2D representations of the calculated orientations are included at the top, while 3D representations below more clearly illustrate both the  $\{01\overline{1}2\}_{\alpha}$  and  $\{11\overline{2}0\}_{\alpha}$  fibers around the solidification direction. The  $\{01\overline{1}2\}_{\alpha}$  fiber has higher intensity than the  $\{11\overline{2}0\}_{\alpha}$ , indicating a stronger preference for this orientation in the simulated transformation conditions. Simulations completed with MTEX 5.70.

This, however, does not explain why a  $\{01\bar{1}2\}_{\alpha}$  or  $\{11\bar{2}0\}_{\alpha}$  fiber would appear over the other. After all, Figure 17b shows the  $\{01\bar{1}2\}_{\alpha}$  fiber is higher intensity than the  $\{11\bar{2}0\}_{\alpha}$  fiber assuming no preset variant selection or other change to the default orientations in Figure 16. Both fibers have been shown here and elsewhere to be indicative of the  $\beta$ -Ti solidification direction in AM builds [8,10]. However, changes in fiber intensity were also observed to correspond to the solid state microstructure formed during cooling. Diffusional microstructures such as  $\alpha + \beta$  colonies have been shown to promote the  $\{01\bar{1}2\}_{\alpha}$  fiber texture, while basketweave and martensitic microstructures promote the  $\{11\bar{2}0\}_{\alpha}$  fiber [8,10]. Curiously, the  $\{01\bar{1}2\}_{\alpha}$  fiber forms off  $\{110\}_{\beta}$  planes 45° off the solidification direction and the  $\{11\bar{2}0\}_{\alpha}$  fiber off  $\{110\}_{\beta}$  planes 90° off the

solidification direction. In simpler terms, the  $\{01\overline{1}2\}_{\alpha}$  fiber forms off the  $\beta$ -Ti's 45<sup>th</sup> parallel, and the  $\{11\overline{2}0\}_{\alpha}$  off the Equator. This can be seen in Figure 17.

This bimodal variant selection is unexpected, and the underlying mechanisms are not understood at this time. It is thought specific transformation planes governing diffusional (colony) and hybrid diffusional-diffusionless (basketweave) transformations may influence the product phase orientations. Plane multiplicity may also influence the involvement of certain planes in different types of solid state phase transformations. Variant selection based on local thermal conditions and stresses may additionally influence the favored solid state orientations. Regardless, future work aims to understand the exact mechanisms of this transformation process and how to further tailor the produced textures for AM builds. This also confirms these fiber textures can act as markers for the microstructural condition in the solid state, should  $\beta$ -Ti be appropriately oriented.

The lack of a significant  $\alpha$ -Ti fiber texture along the solidification direction corresponds well with the millimeter to centimeter  $\beta$ -Ti grains observed in this work. Too few grains were present or freely rotated around the solidification direction to form a  $\{001\}_{\beta}$  fiber texture, instead being primarily constrained to rotated cube textures. Only in Figure 14 was a  $\{01\overline{1}2\}_{\alpha}$  and  $\{11\overline{2}0\}_{\alpha}$  fiber texture clearly present, indicating more  $\beta$ -Ti grains during deposition and the ability for these grains to rotate around the solidification direction. It is suspected a fiber texture indicates the presence of freshly nucleated  $\beta$ -Ti grains considering the lack of one dominant orientation for the solidifying material. Some evidence for fiber textures can also be seen in Figure A 3, where the  $\beta$ -Ti also takes on a nascent  $\{001\}_{\beta}$  fiber texture along the solidification direction. Other cubic metals such as nickel and aluminum will also likely exhibit fiber textures for finer as-solidified grain sizes for the same reasons. This extends the possible application space for this as-solidified grain size indicator to other alloys besides Ti-6Al-4V. Further work calibrating the intensity of fiber textures in the as-built state would be required to develop a quantifiable diagnostic, but the fundamental knowledge should remain the same.

Competitive growth was also shown to quickly remove fibers from the build in both cases, as further up the build height the 12 variant texture returns. This indicates the presence of one large  $\beta$ -Ti grain, not many smaller grains like before. Thus, it can be confidently stated the presence of either the  $\{01\overline{1}2\}_{\alpha}$  or  $\{11\overline{2}0\}_{\alpha}$  fibers around a solidification direction is an indicator of the size of the  $\beta$ -Ti grains.

It is suspected columnar and hybrid columnar-equiaxed solidification is required to form these fibers. Fully equiaxed solidification will be crystallographically constrained to solidifying on  $(001)_{\beta}$  planes, but these poles will *not* be oriented along the build direction. Rather, they will be randomly distributed and produce a lower  $\beta$ -Ti texture. Columnar solidification, involving some degree of epitaxy even if new  $\beta$ -Ti grains are being formed, will still solidify along the  $(001)_{\beta}$  planes, but do so aligned antiparallel to thermal gradients. This orients two  $(001)_{\beta}$  planes with the build direction and produces the textures observed throughout the Ti-6Al-4V AM literature.

In lieu of fibers, one could also look at estimating the solid state microstructural condition solely from the intensity of the  $(01\bar{1}2)_{\alpha}$  and  $(11\bar{2}0)_{\alpha}$  pole figures. A higher intensity of the former should correspond to a greater colony fraction in the microstructure, while the latter would correspond to basketweave or martensitic morphologies. With the majority of the DED build here exhibiting some variant of a basketweave morphology, it is not surprising that the  $(11\bar{2}0)_{\alpha}$  poles

consistently exhibit higher intensity throughout the build. Even at the bottom of the outer rim the  $(11\bar{2}0)_{\alpha}$  exhibits a higher intensity, corresponding to the expected layered microstructure. Thus, rough m.r.d. quantification of both the  $(01\bar{1}2)_{\alpha}$  and  $(11\bar{2}0)_{\alpha}$  poles aligned with the solidification direction could also give an idea on the solid state microstructure, without requiring the presence of a fiber texture and suitably oriented  $\beta$ -Ti. Such logic would be incredibly useful for employing targeted XRD analysis to measure specific planes and expand the application of these findings to more than PBF-EB builds.

Standardization of this diagnostic process is required for further development of this logic. Future work needs to assess how large of an analysis area is required for representative data of both the as-solidified and solid state microstructures. The required duration for a representative XRD scan is also required. For other alloy systems which solidify as a cubic phase (nickel, aluminum, etc.), standardized sampling of the as-solidified orientations could also qualitatively determine microstructural condition. Quantitative evaluation of grain size could subsequently be developed as a capability, but requires further investigation.

It is worth noting the findings reported here originate from a large build volume with unique thermal conditions. Though previous research and the large areas surveyed in this work lend credence to the findings reported here, investigations such as this would additionally benefit from analyzing multiple builds of the same geometry. This would guarantee larger sample sizes to explore unique phenomenon, and is recommended for future research in this area. Duplicate build volumes were not produced here due to equipment constraints, but this is recommended as a best practice moving forward if possible. Build geometries with duplicate "copies" are also key to further developing the relationships between crystallographic texture and microstructural condition outlined here. Natural variations in solidification and phase transformation phenomena can be captured, and a higher fidelity understanding of material response to build conditions can be developed as a result.

# 5. Conclusions

By employing centimeter scale EBSD, neutron diffraction, SEM characterization, and orientation simulations, the following findings were reported in this work.

1) The presence of as-solidified fiber textures along the solidification direction are indicators of parent grain size, while the specific orientation in each solid state phase fiber identifies the type of solid state microstructure present. A mechanistic explanation is proposed explaining how the  $\{01\overline{1}2\}_{\alpha}$  and  $\{11\overline{2}0\}_{\alpha}$  fibers can only exist around the solidification condition *if* more numerous and smaller  $\beta$ -Ti grains are present in the microstructure. The  $\{01\overline{1}2\}_{\alpha}$  and  $\{11\overline{2}0\}_{\alpha}$  fibers correspond to diffusional and non-diffusion dominated microstructures respectively. It is unknown exactly why these orientations indicate different solid state microstructures, but a number of theories are proposed. The fiber textures originating from finer as-solidified grains are also theorized to qualitatively indicate microstructural scale in the as-built condition of other cubic systems such as nickel or aluminum. Analogous fiber textures may also be useful indicators of grain size in traditional manufacturing processes.

- 2)  $\beta$ -Ti was found to solidify preferentially in a rotated cube texture. This rotated cube texture aligned more with the Z-axis build direction at higher build heights.
- 3) The presence of large  $\beta$ -Ti grains is indicated by the lack of either the  $\{01\overline{1}2\}_{\alpha}$ ,  $\{11\overline{2}0\}_{\alpha}$ , or  $(001)_{\beta}$  fiber texture. Rather, a 12 variant  $\alpha$ -Ti texture manifests from large dominant  $\beta$ -Ti grains and localized textures. The intensity of the 12 variant  $\alpha$ -Ti texture corresponds proportionally to the size of  $\beta$ -Ti grains in the DED build.
- 4) The intensity of the  $(011\overline{2})_{\alpha}$  and  $(11\overline{2}0)_{\alpha}$  poles can be used as an analog for the solid state microstructural condition, if fiber textures are not present. These textures also correspond to the solidification direction of *any*  $\beta$ -Ti grains with columnar dendritic characteristics.
- 5) The Burgers OR was consistently followed and accurately reconstructed the as-solidified microstructures for the DED build evaluated here.
- 6) A four-morphology tiered microstructure dominated the as-built microstructure. This consisted of fine basketweave, coarse basketweave, elongated "bow tie" colonies, and high aspect ratio plate colonies formed by differential heating upon additional material being added to the build.
- 7) Large colony microstructures were produced at the build edge and build interior due to insufficient reheating upon subsequent deposition. These regions were also found to be prone to crack propagation, while basketweave morphologies resisted crack growth.
- 8) A *near complete* fracture of the DED Ti-6Al-4V build was observed in regions with large colony microstructures. The crack path for this fracture was explained via basal and prismatic Schmid factors of the  $\alpha$ -Ti phase. Initiation for this fracture and smaller surface cracks was attributed to residual stresses overloading a thin  $\alpha$ -casing found on the build edge from excess oxygen pickup.
- 9) Equiaxed and weld-like  $\beta$ -Ti grains were observed due to build pauses during fabrication. This also produced the formation of the aforementioned large colonies and lead to poor crack resistance.
- 10) Tailoring of DED microstructures for specific crack propagation or crack resistance is possible via controlled thermal histories. Reducing the heating of previous layers can retain initially transformed colony microstructures, and also modify solidification morphology with appropriate changes to scan strategy and other parameters.

# 6. Acknowledgements

AIS gratefully acknowledges the National Science Foundation Graduate Research Fellowship, USA, under Grant No. 2019260337 for supporting this work. All authors thank the Center for Advanced Non-Ferrous Structural Alloys (CANFSA), USA, a National Science Foundation Industry/University Cooperative Research Center (I/UCRC), [Award No. 1624836] at the Colorado School of Mines (Mines), USA, for support completing this work. Scanning electron microscopy work completed here was supported by the National Science Foundation through DMR-1828454. The authors thank SNL (Jessica Buckner, Collin Donoghue, Andrew Kustas, and Shaun Whetten) for producing the build volume analyzed here and contributions to the manuscript. Neutron diffraction measurements were supported by the Los Alamos Neutron Science Center (LANSCE), a NNSA User Facility operated for the US Department of Energy (DOE) by Los

Alamos National Laboratory (LANL). LANL is operated by Triad National Security, LLC, for the National Nuclear Security Administration, USA, of US DOE (Contract No. 89233218CNA000001). JTB also acknowledges support from the National Institute of Standards and Technology, USA, US Department of Commerce, USA, for the acquisition of large-scale EBSD and during the preparation of this manuscript. Sandia National Laboratories is a multimission laboratory managed and operated by National Technology and Engineering Solutions of Sandia LLC, a wholly owned subsidiary of Honeywell International Inc. for the U.S. Department of Energy's National Nuclear Security Administration under contract DE-NA0003525. This paper describes objective technical results and analysis. Any subjective views or opinions that might be expressed in the paper do not necessarily represent the views of the U.S. Department of Energy or the United States Government.

# 7. Appendix A. Supplementary Materials

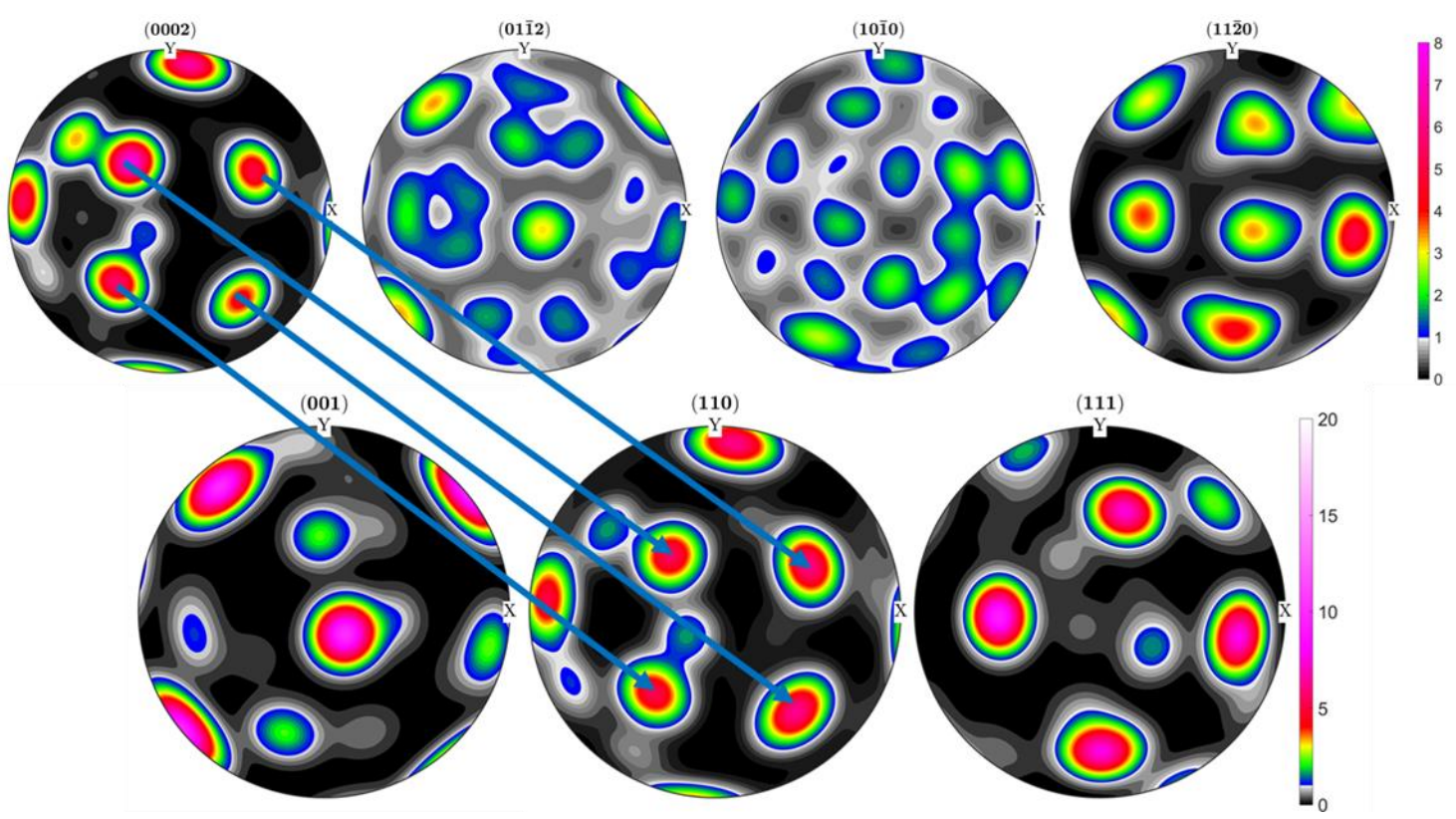


Figure A 1:  $\alpha$ -Ti (top) and  $\beta$ -Ti (bottom) pole figures clearly illustrating the coincident nature of the  $(110)_{\beta}$  and  $(0002)_{\alpha}$  pole figures. This confirms the Burgers OR was dominant in this system. A less obvious but partial correlation also exists with the  $(111)_{\beta}$  and  $(11\bar{2}0)_{\alpha}$  pole figures.

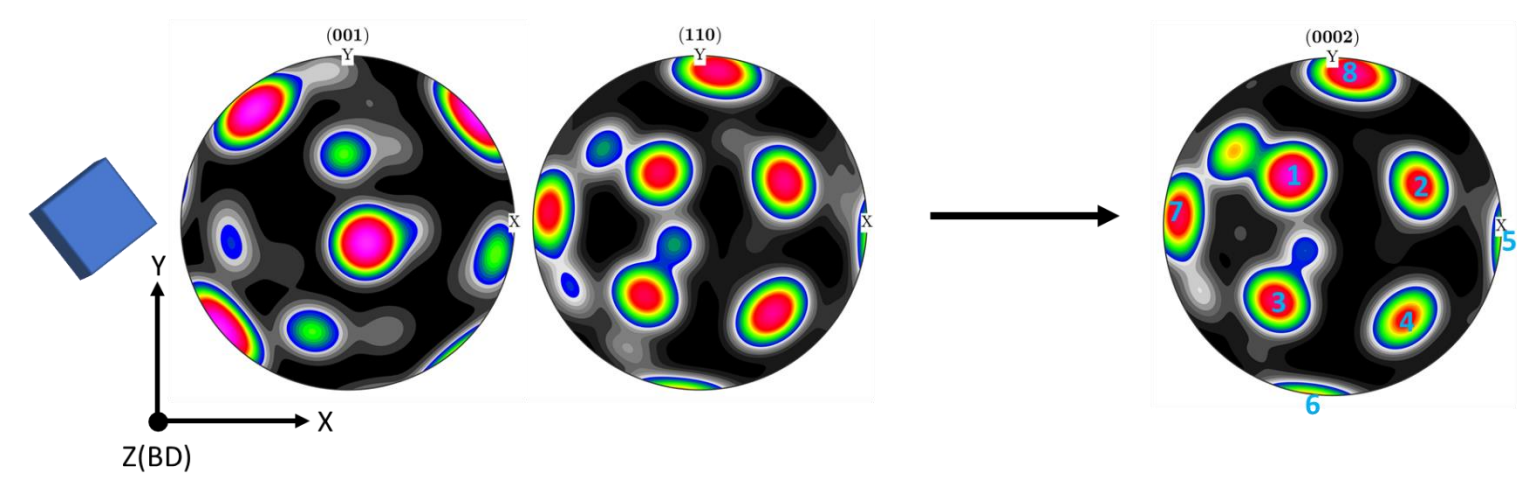


Figure A 2:  $\alpha$ -Ti pole figure (right) illustrating where eight of the possible twelve  $\alpha$ -Ti variants are located when transforming from  $\beta$ -Ti oriented according to the left pole figures. This assumes the Burgers OR is held. Note the correspondence of the  $(110)_{\beta}$  and  $(0002)_{\alpha}$  poles and how the  $(001)_{\beta}$  poles near the build direction align with the center of the square vertices marked by  $\alpha$ -Ti

variants 1-4. Note variants 9-12 have the mirrored orientations of 1-4 in the southern hemisphere of the pole figure.

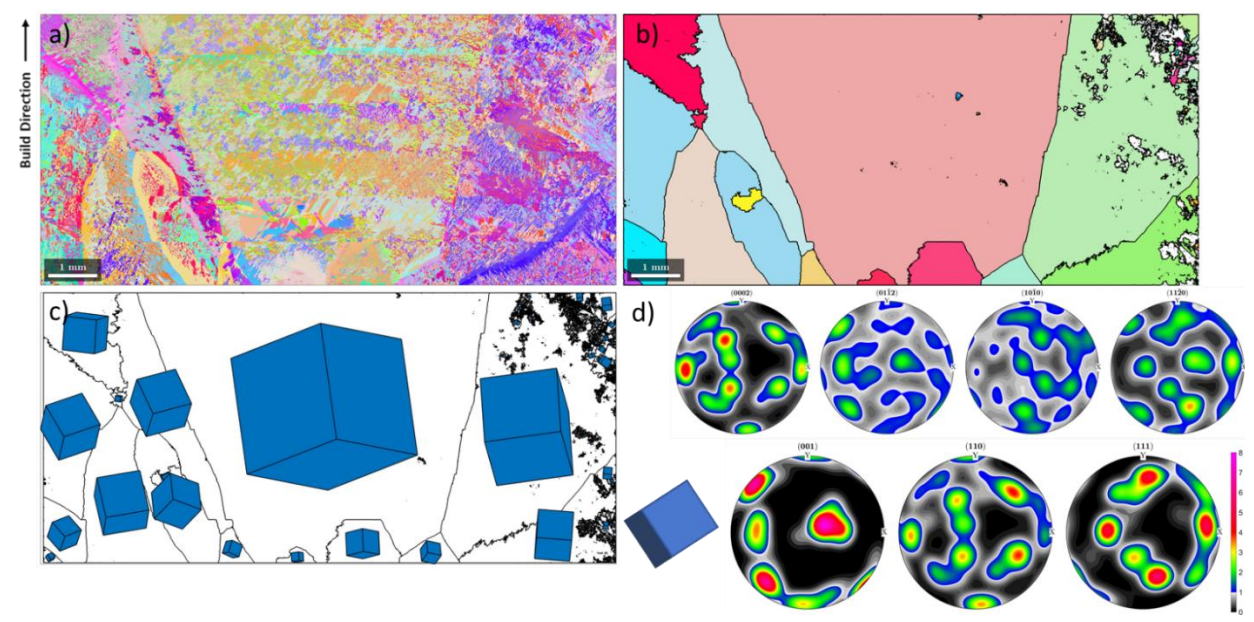


Figure A 3: a)  $\alpha$ -Ti EBSD map of 20-25 mm in build height covering 11 x 5 mm. Regions of  $\alpha$  +  $\beta$  microstructure can be observed towards the bottom of the scanned area, indicating another build pause likely occurred at this build height. All orientations colored with respect to the build height. b) Reconstructed  $\beta$ -Ti microstructure demonstrating the same fanned out columnar grains as Figure 8a with some equiaxed solidification towards the bottom of the map. c) Crystal map of the reconstructed  $\beta$ -Ti grains illustrating a preference for the  $(001)_{\beta}$  poles  $\sim 15^{\circ}$  off the build direction. d)  $\alpha$ -Ti (top) and  $\beta$ -Ti pole figures (bottom) illustrating the preferential alignment of both phases. Note the  $(110)_{\beta}$  and  $(0002)_{\alpha}$  pole figures are nearly identical, demonstrating the Burgers OR was again dominant in the solid state transformation. Partial fiber textures appear in both sets of pole figures.

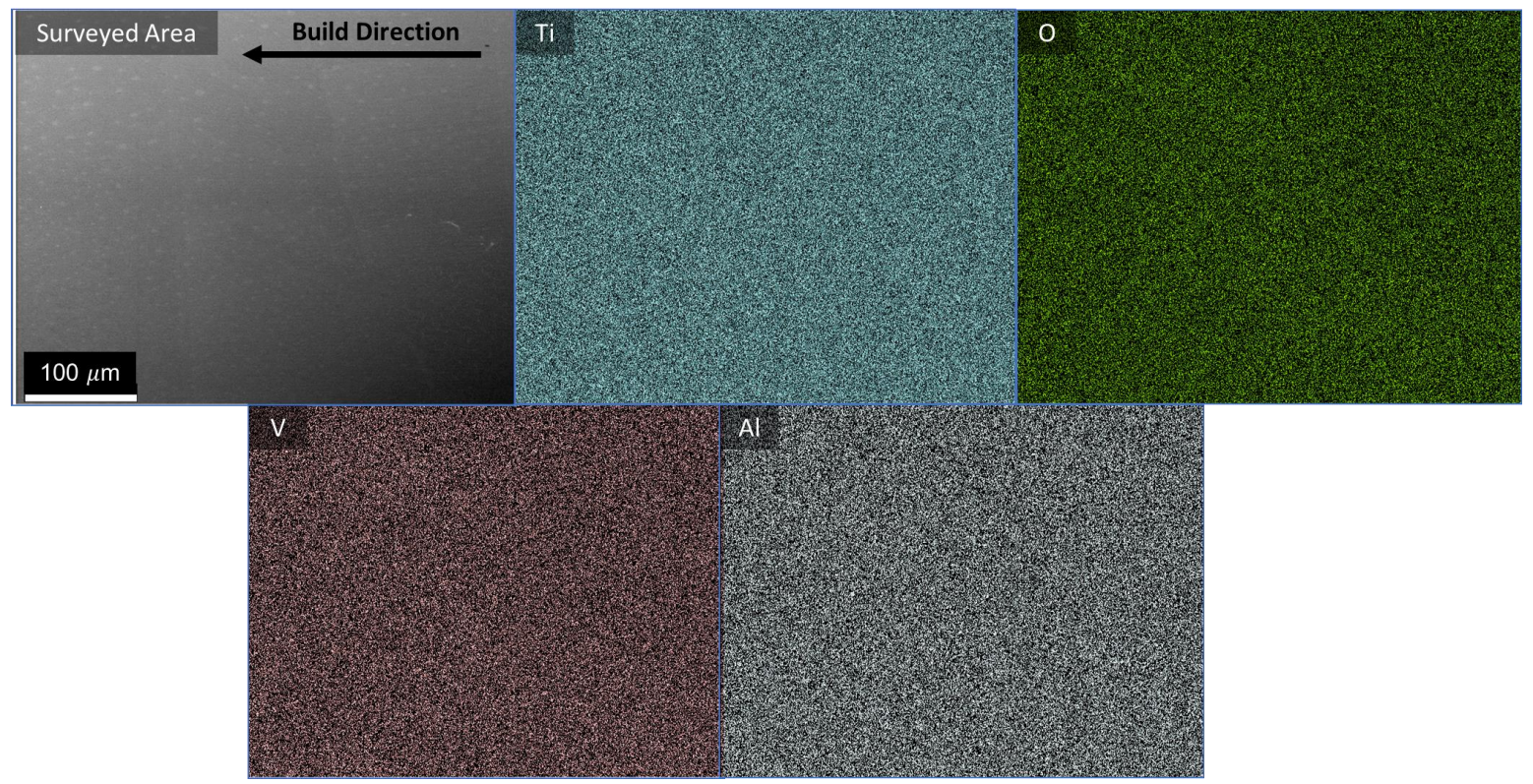


Figure A 4: EDS map of the colony region illustrated in Figure 10 to assess possible inhomogeneous oxygen contamination during the build pause. No remnant oxides or oxygen partitioning was observed, thus suggesting oxygen played a minimal role in the formation of equiaxed  $\beta$ -Ti grains and colony microstructures away from the build surface.



Figure A 5: Video still demonstrating the XY-plane traversal of the deposition process. The central point of the TIG torch never reaches the edge of the build geometry, partially heating both the inner and outer diameters. This results in less heating after initial deposition and the retention of the large colony microstructure. The full video can be seen in Supplementary Materials.

# 8. References

- [1] A. Bhatia, A.K. Sehgal, Additive manufacturing materials, methods and applications: A review, Materials Today: Proceedings. (2021) S2214785321032995. https://doi.org/10.1016/j.matpr.2021.04.379.
- [2] W.E. Frazier, Metal Additive Manufacturing: A Review, Journal of Materials Engineering and Performance. 23 (2014) 1917–1928. https://doi.org/10.1007/s11665-014-0958-z.
- [3] L. Ladani, M. Sadeghilaridjani, Review of Powder Bed Fusion Additive Manufacturing for Metals, Metals. 11 (2021) 1391. https://doi.org/10.3390/met11091391.
- [4] F42 Committee, Terminology for Additive Manufacturing General Principles Terminology, ASTM International, n.d. https://doi.org/10.1520/ISOASTM52900-15.
- [5] W.J. Sames, F.A. List, S. Pannala, R.R. Dehoff, S.S. Babu, The metallurgy and processing science of metal additive manufacturing, International Materials Reviews. 61 (2016) 315–360. https://doi.org/10.1080/09506608.2015.1116649.
- [6] T. DebRoy, H.L. Wei, J.S. Zuback, T. Mukherjee, J.W. Elmer, J.O. Milewski, A.M. Beese, A. Wilson-Heid, A. De, W. Zhang, Additive manufacturing of metallic components Process, structure and properties, Progress in Materials Science. 92 (2018) 112–224. https://doi.org/10.1016/j.pmatsci.2017.10.001.
- [7] B. Blakey-Milner, P. Gradl, G. Snedden, M. Brooks, J. Pitot, E. Lopez, M. Leary, F. Berto, A. du Plessis, Metal additive manufacturing in aerospace: A review, Materials & Design. 209 (2021) 110008. https://doi.org/10.1016/j.matdes.2021.110008.
- [8] A.A. Antonysamy, J. Meyer, P.B. Prangnell, Effect of build geometry on the β-grain structure and texture in additive manufacture of Ti6Al4V by selective electron beam melting, Materials Characterization. 84 (2013) 153–168. https://doi.org/10.1016/j.matchar.2013.07.012.
- [9] M. Simonelli, Y.Y. Tse, C. Tuck, On the Texture Formation of Selective Laser Melted Ti-6Al-4V, Metallurgical and Materials Transactions A. 45 (2014) 2863–2872. https://doi.org/10.1007/s11661-014-2218-0.
- [10] A.I. Saville, S.C. Vogel, A. Creuziger, J.T. Benzing, A.L. Pilchak, P. Nandwana, J. Klemm-Toole, K.D. Clarke, S.L. Semiatin, A.J. Clarke, Texture evolution as a function of scan strategy and build height in electron beam melted Ti-6Al-4V, Additive Manufacturing. 46 (2021) 102118. https://doi.org/10.1016/j.addma.2021.102118.
- [11] C.A. Brice, W.A. Tayon, A.L. Pilchak, Texture Development in Titanium Components Made by Additive Manufacturing, San Diego. (2014) 16.
- [12] T.M. Butler, C.A. Brice, W.A. Tayon, S.L. Semiatin, A.L. Pilchak, Evolution of Texture from a Single Crystal Ti-6Al-4V Substrate During Electron Beam Directed Energy Deposition, Metallurgical and Materials Transactions A. 48 (2017) 4441–4446. https://doi.org/10.1007/s11661-017-4219-2.
- [13] S. Kou, Welding Metallurgy, John Wiley & Sons, Inc., 2002.
- [14] P.A. Kobryn, S.L. Semiatin, The laser additive manufacture of Ti-6Al-4V, JOM. 53 (2001) 40–42. https://doi.org/10.1007/s11837-001-0068-x.
- [15] S.C. Vogel, S. Takajo, M.A. Kumar, E.N. Caspi, A. Pesach, E. Tiferet, O. Yeheskel, Ambient and High-Temperature Bulk Characterization of Additively Manufactured Ti-6Al-4V Using Neutron Diffraction, JOM. 70 (2018) 1714–1722. https://doi.org/10.1007/s11837-018-3038-2.
- [16] A. Pesach, E. Tiferet, S.C. Vogel, M. Chonin, A. Diskin, L. Zilberman, O. Rivin, O. Yeheskel, E.N. Caspi, Texture analysis of additively manufactured Ti-6Al-4V using neutron

- diffraction, Additive Manufacturing. 23 (2018) 394–401. https://doi.org/10.1016/j.addma.2018.08.010.
- [17] H.L. Wei, J. Mazumder, T. DebRoy, Evolution of solidification texture during additive manufacturing, Scientific Reports. 5 (2015). https://doi.org/10.1038/srep16446.
- [18] S.S. Al-Bermani, M.L. Blackmore, W. Zhang, I. Todd, The Origin of Microstructural Diversity, Texture, and Mechanical Properties in Electron Beam Melted Ti-6Al-4V, Metallurgical and Materials Transactions A. 41 (2010) 3422–3434. https://doi.org/10.1007/s11661-010-0397-x.
- [19] S. Mereddy, Grain refinement of wire arc additively manufactured titanium by the addition of silicon, Journal of Alloys and Compounds. (2017) 7.
- [20] M.J. Bermingham, Effect of trace lanthanum hexaboride and boron additions on microstructure, tensile properties and anisotropy of Ti-6Al-4V produced by additive manufacturing, Materials Science. (2018) 11.
- [21] Q. Wang, K. Zhang, D. Qiu, W. Niu, Additive manufacturing of high-strength commercially pure titanium through lanthanum oxide addition, Materials Characterization. (2021) 111074. https://doi.org/10.1016/j.matchar.2021.111074.
- [22] J.R. Kennedy, A.E. Davis, A.E. Caballero, N. Byres, S. Williams, E.J. Pickering, P.B. Prangnell, β Grain refinement by yttrium addition in Ti-6Al-4V Wire-Arc Additive Manufacturing, Journal of Alloys and Compounds. 895 (2022) 162735. https://doi.org/10.1016/j.jallcom.2021.162735.
- [23] S.A. Mantri, T. Alam, D. Choudhuri, C.J. Yannetta, C.V. Mikler, P.C. Collins, R. Banerjee, The effect of boron on the grain size and texture in additively manufactured β-Ti alloys, Journal of Materials Science. 52 (2017) 12455–12466. https://doi.org/10.1007/s10853-017-1371-4.
- [24] R.A. Rahman Rashid, S. Palanisamy, H. Attar, M. Bermingham, M.S. Dargusch, Metallurgical features of direct laser-deposited Ti6Al4V with trace boron, Journal of Manufacturing Processes. 35 (2018) 651–656. https://doi.org/10.1016/j.jmapro.2018.09.018.
- [25] S.A. Mantri, T. Torgerson, E. Ivanov, T.W. Scharf, R. Banerjee, Effect of Boron Addition on the Mechanical Wear Resistance of Additively Manufactured Biomedical Titanium Alloy, Metallurgical and Materials Transactions A. 49 (2018) 806–810. https://doi.org/10.1007/s11661-017-4454-6.
- [26] P.L. Stephenson, N. Haghdadi, R. DeMott, X.Z. Liao, S.P. Ringer, S. Primig, Effect of scanning strategy on variant selection in additively manufactured Ti-6Al-4V, Additive Manufacturing. 36 (2020) 101581. https://doi.org/10.1016/j.addma.2020.101581.
- [27] M. Shao, S. Vijayan, P. Nandwana, J.R. Jinschek, The effect of beam scan strategies on microstructural variations in Ti-6Al-4V fabricated by electron beam powder bed fusion, Materials & Design. 196 (2020) 109165. https://doi.org/10.1016/j.matdes.2020.109165.
- [28] L. Sun, X. Ren, J. He, Z. Zhang, A bead sequence-driven deposition pattern evaluation criterion for lowering residual stresses in additive manufacturing, Additive Manufacturing. 48 (2021) 102424. https://doi.org/10.1016/j.addma.2021.102424.
- [29] W. Zhang, M. Tong, N.M. Harrison, Scanning strategies effect on temperature, residual stress and deformation by multi-laser beam powder bed fusion manufacturing, Additive Manufacturing, 36 (2020) 101507. https://doi.org/10.1016/j.addma.2020.101507.
- [30] W.G. Burgers, On the process of transition of the cubic-body-centered modification into the hexagonal-close-packed modification of zirconium, Physica. 1 (1934) 561–586. https://doi.org/10.1016/S0031-8914(34)80244-3.

- [31] B. McArthur, Effects of Thermal Processing Variations on Microstructure and High Cycle Fatigue of Beta-STOA Ti-6Al-4V, (n.d.) 82.
- [32] Y. Ji, L. Chen, L.-Q. Chen, Understanding Microstructure Evolution During Additive Manufacturing of Metallic Alloys Using Phase-Field Modeling, in: Thermo-Mechanical Modeling of Additive Manufacturing, Elsevier, 2018: pp. 93–116. https://doi.org/10.1016/B978-0-12-811820-7.00008-2.
- [33] M. Motyka, Martensite Formation and Decomposition during Traditional and AM Processing of Two-Phase Titanium Alloys—An Overview, Metals. 11 (2021) 481. https://doi.org/10.3390/met11030481.
- [34] E. Sallica-Leva, R. Caram, A.L. Jardini, J.B. Fogagnolo, Ductility improvement due to martensite α' decomposition in porous Ti–6Al–4V parts produced by selective laser melting for orthopedic implants, Journal of the Mechanical Behavior of Biomedical Materials. 54 (2016) 149–158. https://doi.org/10.1016/j.jmbbm.2015.09.020.
- [35] W. Xu, M. Brandt, S. Sun, J. Elambasseril, Q. Liu, K. Latham, K. Xia, M. Qian, Additive manufacturing of strong and ductile Ti–6Al–4V by selective laser melting via in situ martensite decomposition, Acta Materialia. 85 (2015) 74–84. https://doi.org/10.1016/j.actamat.2014.11.028.
- [36] J. Donoghue, A.A. Antonysamy, F. Martina, P.A. Colegrove, S.W. Williams, P.B. Prangnell, The effectiveness of combining rolling deformation with Wire–Arc Additive Manufacture on β-grain refinement and texture modification in Ti–6Al–4V, Materials Characterization. 114 (2016) 103–114. https://doi.org/10.1016/j.matchar.2016.02.001.
- [37] Standard Terminology for Additive Manufacturing—Coordinate Systems and Test Methodologies, (2019).
- [38] A.I. Saville, A. Creuziger, E.B. Mitchell, S.C. Vogel, J.T. Benzing, J. Klemm-Toole, K.D. Clarke, A.J. Clarke, MAUD Rietveld Refinement Software for Neutron Diffraction Texture Studies of Single- and Dual-Phase Materials, Integr Mater Manuf Innov. 10 (2021) 461–487. https://doi.org/10.1007/s40192-021-00224-5.
- [39] F. Bachmann, R. Hielscher, H. Schaeben, Texture Analysis with MTEX Free and Open Source Software Toolbox, Solid State Phenomena. 160 (2010) 63–68. https://doi.org/10.4028/www.scientific.net/SSP.160.63.
- [40] D. Mainprice, F. Bachmann, R. Hielscher, H. Schaeben, Descriptive tools for the analysis of texture projects with large datasets using MTEX: strength, symmetry and components, Geological Society, London, Special Publications. 409 (2015) 251–271. https://doi.org/10.1144/SP409.8.
- [41] F. Niessen, T. Nyyssönen, A.A. Gazder, R. Hielscher, Parent grain reconstruction from partially or fully transformed microstructures in MTEX, ArXiv:2104.14603 [Cond-Mat]. (2021). http://arxiv.org/abs/2104.14603 (accessed May 24, 2021).
- [42] H.J. Bunge, Texture Analysis in Materials Science, Elsevier, 1982. https://doi.org/10.1016/C2013-0-11769-2.
- [43] S.M. Kelly, S.L. Kampe, Microstructural evolution in laser-deposited multilayer Ti-6Al-4V builds: Part I. Microstructural characterization, Metall and Mat Trans A. 35 (2004) 1861–1867. https://doi.org/10.1007/s11661-004-0094-8.
- [44] O. Zinovieva, A. Zinoviev, V. Ploshikhin, Three-dimensional modeling of the microstructure evolution during metal additive manufacturing, Computational Materials Science. 141 (2018) 207–220. https://doi.org/10.1016/j.commatsci.2017.09.018.

- [45] Z. Zhang, Z.J. Tan, X.X. Yao, C.P. Hu, P. Ge, Z.Y. Wan, J.Y. Li, Q. Wu, Numerical methods for microstructural evolutions in laser additive manufacturing, Computers & Mathematics with Applications. 78 (2019) 2296–2307. https://doi.org/10.1016/j.camwa.2018.07.011.
- [46] S. Liu, Y.C. Shin, Integrated 2D cellular automata-phase field modeling of solidification and microstructure evolution during additive manufacturing of Ti6Al4V, Computational Materials Science. 183 (2020) 109889. https://doi.org/10.1016/j.commatsci.2020.109889.
- [47] S. Sahoo, K. Chou, Phase-field simulation of microstructure evolution of Ti–6Al–4V in electron beam additive manufacturing process, Additive Manufacturing. 9 (2016) 14–24. https://doi.org/10.1016/j.addma.2015.12.005.
- [48] Y. Xie, M. Gong, Z. Luo, Q. Li, M. Gao, F. Wang, X. Zeng, G. Wang, Effect of microstructure on short fatigue crack growth of wire arc additive manufactured Ti-6Al-4V, Materials Characterization. 177 (2021) 111183. https://doi.org/10.1016/j.matchar.2021.111183.
- [49] C. Li, Z.Y. Liu, X.Y. Fang, Y.B. Guo, Residual Stress in Metal Additive Manufacturing, Procedia CIRP. 71 (2018) 348–353. https://doi.org/10.1016/j.procir.2018.05.039.
- [50] M.J. Bermingham, S.D. McDonald, D.H. StJohn, M.S. Dargusch, Beryllium as a grain refiner in titanium alloys, Journal of Alloys and Compounds. 481 (2009) L20–L23. https://doi.org/10.1016/j.jallcom.2009.03.016.
- [51] Z. Lin, K. Song, X. Yu, A review on wire and arc additive manufacturing of titanium alloy, Journal of Manufacturing Processes. 70 (2021) 24–45. https://doi.org/10.1016/j.jmapro.2021.08.018.
- [52] K.S. Chan, M. Koike, B.W. Johnson, T. Okabe, Modeling of Alpha-Case Formation and Its Effects on the Mechanical Properties of Titanium Alloy Castings, Metall and Mat Trans A. 39 (2008) 171–180. https://doi.org/10.1007/s11661-007-9406-0.